Received: 31 August 2017 | Revised: 14 March 2018 | Accepted: 15 March 2018

DOI: 10.1002/nme.5807

RESEARCH ARTICLE

WILEY

Variational inequality-based framework of discontinuous deformation analysis

Huo Fan[1] | Jidong Zhao[1] | Hong Zheng[2]

[1]Department of Civil and Environmental Engineering, The Hong Kong University of Science and Technology, Kowloon, Hong Kong

[2]Key Laboratory of Urban Security and Disaster Engineering, Ministry of Education, Beijing University of Technology, Beijing, China

Correspondence
Huo Fan, Department of Civil and Environmental Engineering, The Hong Kong University of Science and Technology, Kowloon, Hong Kong.
Email: huofan_hkust@163.com; jzhao@ust.hk

Funding information
University Grants Council of Hong Kong through a Collaborative Research Fund (CRF), Grant/Award Number: C6012-15G; National Basic Research Program of China, Grant/Award Number: 2014CB047100; National Natural Science Foundation of China, Grant/Award Number: 11172313 and 51538001

Summary

For modeling discrete particle-block systems, a new framework of discontinuous deformation analysis is established on the basis of finite-dimensional variational inequality. The presented method takes into account the contacts, the rolling resistance, and the tensile resistance of cemented interface among particles and blocks using the corresponding variational or quasivariational inequalities. The new formulation avoids using the artificial springs that are usually indispensable in many conventional methods dealing with similar discrete problems and conveniently integrates the rigid circle particles, the nonrigid ring particles, and the arbitrary shape blocks into a uniform framework. The proposed discontinuous deformation analysis approach is further coupled with the finite element method using a node-based composite contact matrix and several simple transformation matrices to solve practical problems. A particle/block-based composite contact matrix is constructed to further broaden the application of the proposed method. The accuracy, robustness, and capability of the presented method are demonstrated with examples.

KEYWORDS

contact nonlinearity, discontinuous deformation analysis, projection-contraction algorithm, rolling resistance, variational inequality

1 | INTRODUCTION

Discrete particle or block systems are commonly encountered in various engineering problems in civil, mechanical and chemical engineering, and mining industry. The mechanical responses in such systems are widely regarded complicated and challenging to characterize and model. They may include not only multibody interactions but also fluid-solid coupling and sometimes cross-scale interactions as well. Historically, there have been a wide variety of theories developed for analyzing such discrete particle/block systems, including fluid dynamics, granular mechanics, soil mechanics, rock mechanics, and powder technology. Indeed, discrete systems can range from very small to large length scales and can be tackled by different approaches. For example, the molecular dynamics method[1-6] has been proposed to model the physical movements and interactions of atoms and molecules. The lattice Boltzmann method[7-11] has been widely employed to simulate the evolution of a fluid system through modeling the collisions and propagations of fictive particles over a discrete lattice mesh. Meanwhile, the discrete element method (DEM)[12-16] has been particularly popular in simulating engineering materials such as granular sands. The DEM typically treats a material as an assembly of discrete particles interacting with one another through interparticle contacts and frictions and solve the Newton's equations of motion governing the

particle system.[17] In addition, the combined finite DEM,[18-25] the particle method, and the corresponding contact algorithm[26-28] have been presented. The related developments and applications of these methods can be found in monographs.[29,30]

In parallel with the aforementioned discrete methods, the discontinuous deformation analysis (DDA)[31] has also received much attention in analyzing discrete block/particle systems, in particular in application for civil/rock engineering. Discontinuous deformation analysis is sometimes categorized as a special class of DEM, but it solves a boundary stress-displacement problem based on the principle of minimum potential energy (or by Hamilton's principle) similar to the finite element method (FEM). To improve its capacity in coping with deformation, the nodal-based DDA[32] and the coupled FEM-DDA approach[33] have been proposed. In dealing with geometrical nonlinearity, various forms of extension on DDA have been proposed, including those based on the postadjustment method,[34] the Taylor series method,[35] the trigonometric method,[36] the displacement-strain modification method,[37] and the strain-rotation (SR)–DDA[38,39] based on the SR decomposition theorem.[40-42] In particular, the SR-DDA formulation helps to void the small deformation assumption. The issue of contact nonlinearity has been tackled more recently by such methods including the open-close iteration (OCI),[31] the augmented Lagrange multiplier method,[43] the Lagrange multiplier method,[44] the complementarity method,[45-47] and the variational inequality method.[48] Other latest developments in DDA include the angle-based method[49] in addressing the indeterminacy of vertex-vertex contact, the new contact theory,[50] and the generalized contact potential-based DDA[51] to address the potential contact.

In the original framework of DDA, a circle particle is commonly approximated by an equilateral polygon, which inevitably increases the computational cost when the simplex integration[52] is used. The subsequent developments of rigid particle DDA,[53] the nonrigid particle DDA,[54] and the rigid block DDA[55] still adopt the penalty method and the OCI scheme and have to deal with the contact nonlinearity. The penalty method depends heavily on the stiffness of artificial contact spring, whose value, however, is difficult to determine and is usually problem dependent. Thus, it is not always to obtain the correct contact forces for all cases. In a typical OCI, the contact springs are repeatedly installed and removed from the specific contact points to reflect the change of contact states, ie, either opening or closing. Accordingly, the governing equation needs to be constantly reformed and resolved. The OCI scheme may thus cause dramatic decrease in computational efficiency with the increasing number of contact pairs, and more importantly, no theory has been established to ensure the convergence result obtained from the OCI to the final correct contact states. In addition, the OCI may lead to nonphysical complications among the contact nonlinearity, the geometrical nonlinearity, and the material nonlinearity. Meanwhile, the recent developments of the theory of finite-dimensional quasivariational inequality and the dual formulation of DDA (called DDA-d)[56] render the artificial springs totally dispensable for both the normal and shear contacts and make the OCI unnecessary as well. While it has been demonstrated that the DDA-d has attained much improved accuracy, robustness, and acceptable efficiency as compared with previous formulations, it still needs to use the equilateral polygon to approximate the circle particle and has to rely on an assumption of constant strain and constant stress inside of a block. Moreover, it remains a pending problem in the DDA-d to simulate the behavior of rock bolt, which is the required function of the original DDA. Moreover, an unphysical phenomenon of "one-step lag" (to be explained in detail in Section 4.3) exists in the DDA-d.

In this study, ***first***, considering the independence between the shape of block and the basic unknowns in DDA, we extend the interpolation shape function of the circle particle to ring particle. In doing so, the rigid and nonrigid circles or ring particle, the arbitrary shape rigid and nonrigid block can all be integrated together to construct a new DDA framework. Moreover, the tactics of "double contact displacement" is proposed to overcome the aforementioned unphysical phenomenon of "one-step lag." ***Second***, applying the concept of instantaneous center of rotation in theoretical mechanics, the rolling resistance is translated into an equivalent variational inequality formulation. Meanwhile, the mechanical behavior of cemented interface is described by the quasivariational inequality and the normal and shear contacts. Consequently, the artificial springs can be totally abandoned in 4 cases of normal contact, shear contact, rolling resistance, and tensile resistance of cemented interface. For simplicity, the new DDA framework will be abbreviated as particle-block (PB)–DDA in the sequel to highlight its capability of simulating complicated particle-block systems. ***Third***, to accommodate cases where the particle or block needs to be further discreted, a node-based composite contact matrix is formulated to facilitate effective coupling between DDA and FEM, and meanwhile, it may help improve the accuracy of stress and strain of individual particle or block. Indeed, the DDA and the FEM share a common basis of the principle of minimum potential energy, which inspires us to introduce the FEM formula governing link/bolt, spring, and beam element directly into the PB-DDA. Therefore, the link/bolt, spring, and beam become the connectors between particles or blocks. To simulate the behavior of these connectors, ***whereafter***, we construct a particle/block-based composite contact matrix, which allows other models to be implemented in the PB-DDA with ease, including the bonded particle model,[57,58] the

clumped particle model,[59] and the bonded block model.[60] The aforementioned enrichments greatly broaden the potential applications of the PB-DDA, which will be demonstrated with examples in the following sections.

2 | DISPLACEMENT APPROXIMATION

Consider a 2D rigid body with an arbitrary geometrical shape, as shown in Figure 1. The displacement of an arbitrary point A in the body can be described by its rotation about a certain axis passing through a reference point C and the translation of the body. The basic unknown vector is assumed as follows:

$$\mathbf{d} = [u_0, v_0, \theta]^{\mathrm{T}}, \tag{1}$$

where u_0 and v_0 are the translational displacement of reference point of a particle or block in the x and y direction, respectively. θ is the rotation angle of the rigid body about the axis passing through the reference point C, which is assumed to be the geometric centroid of a particle or block in this study. The displacement $\mathbf{u}(x, y)$ of any point A can be expressed as

$$\mathbf{u}(x, y) = \begin{bmatrix} u_x(x, y) \\ u_y(x, y) \end{bmatrix} = \mathbf{T}(x, y)\mathbf{d}, \tag{2}$$

where (x, y) is the coordinate of point A and the interpolation shape function $\mathbf{T}(x, y)$ is given by

$$\mathbf{T}(x, y) = \begin{bmatrix} 1 & 0 & y_c - y \\ 0 & 1 & x - x_c \end{bmatrix}, \tag{3}$$

where (x_c, y_c) is the coordinate of point C. In the framework of DDA, a rigid body with complex geometry can be presented straightforward with its shape features, without resorting to the use of many particles to approximate its profile in other approaches such as DEM.

Now, we further consider a particle or a ring-shaped body (which can be regarded as a particle with a nonzero inner diameter), which can only exhibit volumetric deformation without shear strain. The following basic unknown vector can be adopted:

$$\mathbf{d} = [u_0, v_0, \theta, \varepsilon]^{\mathrm{T}}, \tag{4}$$

where ε is the Cauchy strain and $\varepsilon_x = \varepsilon_y = \varepsilon$ in this case. Accordingly, the interpolation shape function can be expressed

$$\mathbf{T}(x, y) = \begin{bmatrix} 1 & 0 & y_c - y & x - x_c \\ 0 & 1 & x - x_c & y - y_c \end{bmatrix}. \tag{5}$$

For a deformable block of arbitrary shape, the basic unknown vector can be written as

$$\mathbf{d} = \left[u_0, v_0, \theta, \varepsilon_x, \varepsilon_y, \gamma_{xy}\right]^{\mathrm{T}}, \tag{6}$$

where ε_x, ε_y, and γ_{xy} are the 3 Cauchy strain components. The corresponding interpolation shape function is

$$\mathbf{T}(x, y) = \begin{bmatrix} 1 & 0 & y_c - y & x - x_c & 0 & \frac{y - y_c}{2} \\ 0 & 1 & x - x_c & 0 & y - y_c & \frac{x - x_c}{2} \end{bmatrix}. \tag{7}$$

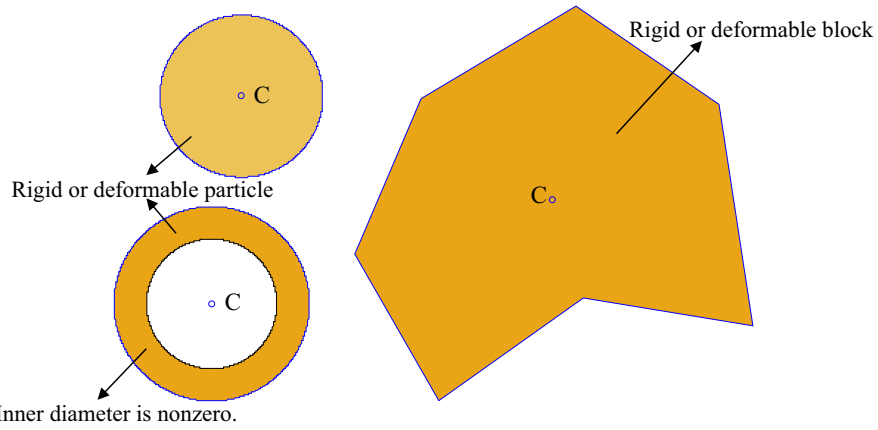

FIGURE 1 Geometrical shapes of rigid or deformable body [Colour figure can be viewed at wileyonlinelibrary.com]

The interpolation functions in Equations (3), (5), or (7) are all first-order functions of x and y. The interpolation shape function and the basic unknown vector constitute the bases for establishing the control equation of motion of a body.

3 | CONTACT TYPES

Major contact types considered in our method include, but not limited to, the particle-particle contact (P–P contact), the particle-block contact (P-B contact), the block-block contact (B-B contact), and the loop–loop contact (L-L contact), each of which is discussed as follows.

For particle-particle contacts, we consider the following 2 cases. Case I occurs when 2 particles are considered "outside" to each other (eg, Figure 2A); Case II occurs when particle P_i is inside of particle P_j whose inner diameter is nonzero, as shown in Figure 2B. The centroid line P_iP_j intersects particles P_i and P_j at points C_i and C_j, respectively, where i and j are the global indexes of the 2 particles. If the distance between C_i and C_j is less than a specified threshold d_0, particles P_i and P_j are considered to be in contact, and this contact can marked as contact pair C_i-$C_{j\text{-PP}}$, where the subscript "PP" indicates that the contact is a particle-particle contact. The midpoint of points C_i and C_j is defined as the contact point C. Line AB passes through the contact point C and is perpendicular to line P_iP_j. It is defined as the contact surface. The unit vector $\mathbf{n}$ from point C to point P_i is defined as the unit normal vector of the contact pair. For convenience in programming, we take the index i is less than the index j, namely, $i<j$. Thus, the unit vector $\mathbf{n}$ points toward the interior of particle with the smaller index. The unit shear vector $\boldsymbol{\tau}$ of the same contact pair is defined by rotating $\mathbf{n}$ clockwise, as shown in Figure 2.

For particle-block contacts, 4 cases, as shown in Figure 3, are considered. Case I: Particle P_i contacts the edge V_iV_j of block B_j from the outside of the block (see Figure 3A); Case II: Particle P_i contacts block B_j from the inside of the block (see Figure 3B); Cases III and IV: The vertex V_j of block B_j contacts particle P_i from either the outside of inside of the particle, as shown in Figure 3C and 3D, respectively. In cases I and II, if the distance C_iC_j between particle and block is less than a specified threshold d_0, these contacts will occur and are termed as C_i-$V_iV_{j\text{-PB}}$, where the subscript "PB" denotes a particle-block contact. The midpoint of line C_i and C_j is defined as the contact point C, and line DE paralleling to edge V_iV_j and passing through point C is defined as the contact surface, as shown in Figure 3A and 3B. For cases III and IV, if the distance between point C_i and vertex V_j is less than d_0, such a contact will occur and is termed as C_i-$V_{j\text{- PB}}$. The contact surface DE is perpendicular to line P_iV_j and passes through the contact point C defined by the midpoint of line C_iV_j, as shown in Figure 3C and 3D. The unit normal vector $\mathbf{n}$ is perpendicular to line DE and points to the interior of particle P_i. By rotating $\mathbf{n}$ clockwise, we can obtain the unit shear vector $\boldsymbol{\tau}$, as shown in Figure 3.

Three contact types between blocks are considered in the original DDA, namely, the vertex-edge contact, the edge-edge contact, and the vertex-vertex contact. Among the 3, the vertex-edge contact is considered the most basic one, while the latter 2 types can be ultimately translated into the vertex-edge contact, as shown in Figure 4. Point V* is the projection of vertex V_k belonging to block B_i on edge V_iV_j of block B_j. If the distance between points V_k and V* is less than d_0,

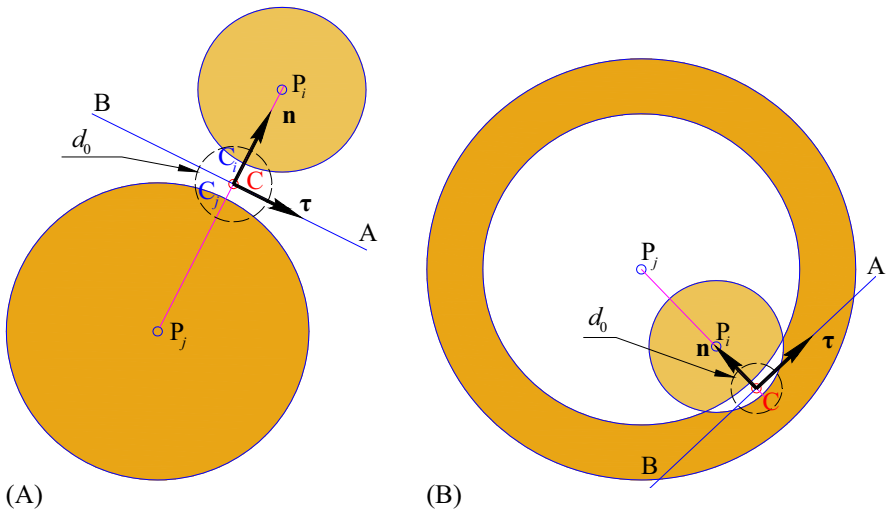

FIGURE 2 Particle-particle contacts. A, Case I; B, Case II [Colour figure can be viewed at wileyonlinelibrary.com]

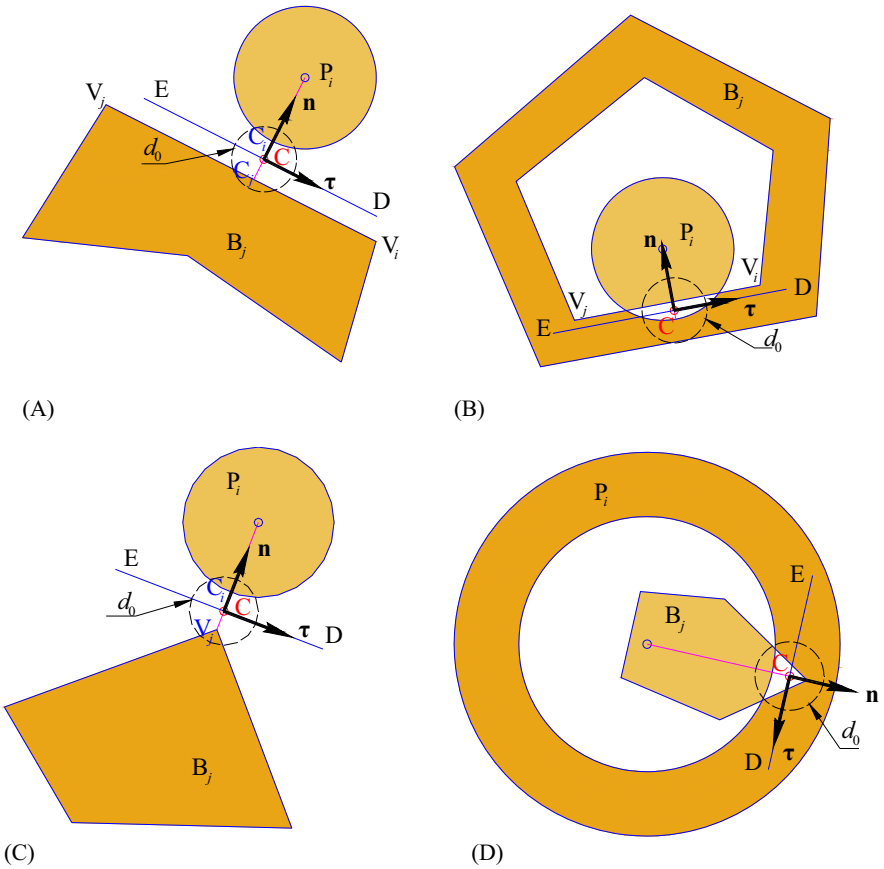

FIGURE 3 Particle-block contacts. A, Case I; B, Case II; C, Case III; D, Case IV [Colour figure can be viewed at wileyonlinelibrary.com]

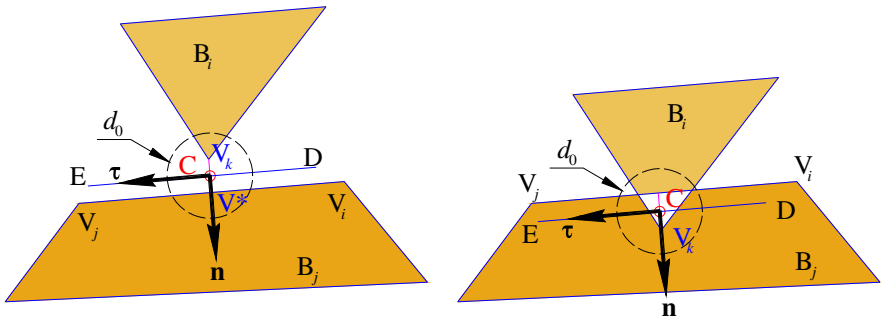

FIGURE 4 Vertex-edge contact of the block-block contact [Colour figure can be viewed at wileyonlinelibrary.com]

the contact pair V_k-$V_iV_{j\text{-BB}}$ is detected, where the subscript "BB" stands for the block-block contact. The midpoint of line V_kV^* is defined as the contact point C. It should be pointed out that vertexes V_k and V^* are the 2 contact points belonging to blocks B_i and B_j, respectively, in the original DDA, and vertex V_k and vertex V^* are thereby considered separate points. In reality, once contacted, the contact point can be regarded as 1 single point for the 2 contact bodies. In this study, midpoint C is defined as the contact point. Indeed, blocks B_i and B_j may own contact point C simultaneously, which has been validated by numerical simulations. The contact surface DE is parallel to edge V_iV_j and passing through point C. The unit normal vector $\mathbf{n}$ is perpendicular to line DE and points to the interior of block B_j, which possesses edge V_iV_j. By rotating $\mathbf{n}$ clockwise, the unit shear vector $\boldsymbol{\tau}$ can be obtained, as shown in Figure 4.

Figure 5 shows the edge-edge contact. If the distances between vertexes V_k, V_l, and edge V_iV_j are all less than d_0 (the left of Figure 5) or the distances between vertexes V_k and V_i and edges V_iV_j and V_kV_l are all less than d_0 (the right of Figure 5), the edge-edge contact V_kV_l-$V_iV_{j\text{-BB}}$ is considered to occur, and it is further translated into 2 pair of vertex-edge contacts, namely, the vertex-edge contacts V_k-$V_iV_{j\text{-BB}}$ and V_l-$V_iV_{j\text{-BB}}$ (the left of Figure 5) or the vertex-edge contacts V_k-$V_iV_{j\text{-BB}}$ and

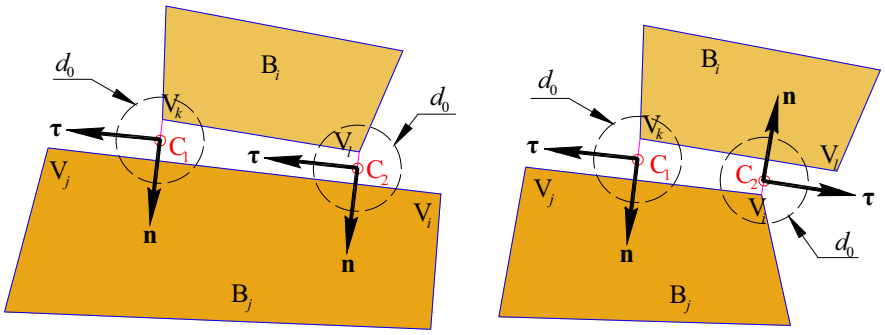

FIGURE 5 Edge-edge contact of the block-block contact [Colour figure can be viewed at wileyonlinelibrary.com]

V_i-$V_kV_{l\text{-BB}}$ (the right of Figure 5). In this case, one of the contact pairs is called as the "adjoint contact pair" of the other contact pair. The vertex-edge contact V_k-$V_iV_{j\text{-BB}}$ or V_i-$V_kV_{l\text{-BB}}$, is called "adjoint vertex-edge contact".

As for the vertex-vertex contact, one needs first to identify the 2 candidate contact edges and then to select 1 edge and 1 vertex according to the geometrical relationship to form a vertex-edge contact. Accordingly, the treatment of vertex-vertex hereby adopted is the same as the way in the original DDA.

To account for deformability, a block can be subdivided into elements. In this case, the boundary of the block is called the loop, as shown in Figure 6. Both blocks B_i and B_j are subdivided. If there is a contact between the 2 blocks, the contact is referred to as the loop-loop contact (L-L contact). Since elements E_k^i and E_k^j can be regarded as 2 smaller blocks, the loop-loop contact can be treated as a block-block contact. Apparently, depending on different circumstances, there may be particle-loop contacts (P-L contacts) and block-loop contacts (B-L contacts) in a discrete particle-block system, as shown in Figure 7. The former can be treated as the particle-block contacts, while the latter can be tackled as the block-block contacts.

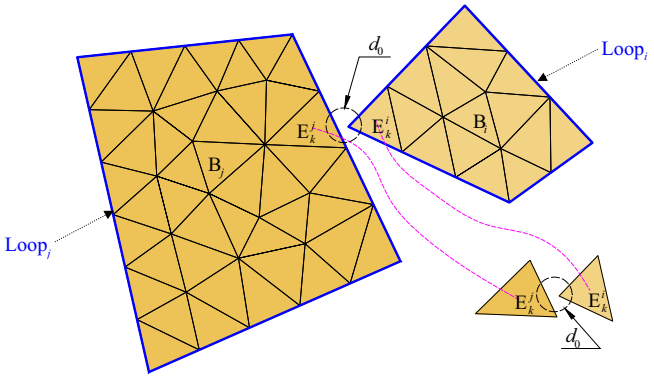

FIGURE 6 A loop-loop contact [Colour figure can be viewed at wileyonlinelibrary.com]

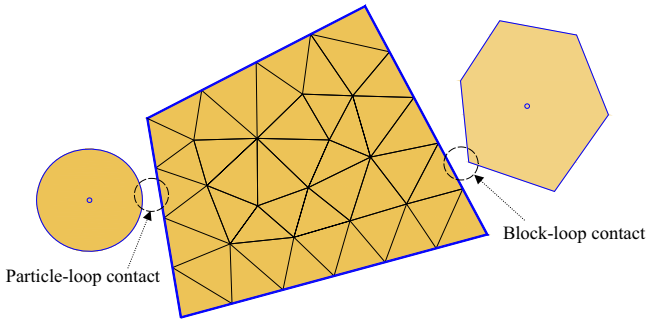

FIGURE 7 Particle-loop contact and block-loop contact [Colour figure can be viewed at wileyonlinelibrary.com]

4 | DISCONTINUOUS DEFORMATION ANALYSIS UNDER THE FRAMEWORK OF THE VARIATIONAL INEQUALITY

Variational inequality has been employed in treating the Signorini problem,[61] and its application in DDA can be found in the work of Jiang and Zheng,[48] while detailed theory about variational inequality can be referred to the work of Facchinei and Pang[62]; here, we will offer the equivalent formulations of the contact conditions, the rolling resistance, and the tension resistance of the cemented interface under the framework of the variational inequality. For completeness, the governing equation of a single body (particle or block) motion is briefly discussed.

4.1 | Governing equation of a body motion

Consider a rigid or deformable block B_i, as shown in Figure 8. The centroid of the block is located at point C. In this Figure, **G** denotes the body force; **F**, **P**, and **u** are the specified point loading, surface loading, and displacement constraint, respectively. The vertexes V_k and V_m are the contact points and the unit vertors $\mathbf{n}_k$, $\boldsymbol{\tau}_k$, and $\mathbf{n}_m$; $\boldsymbol{\tau}_m$ corresponds to the kth and the mth contact pairs, respectively. According to the definitions for the unit normal and shear vector and the laws of action and reaction, the contact force $(p_k^n\mathbf{n}_k, p_k^\tau\boldsymbol{\tau}_k)$ acts on edge V_iV_j of block B_i, while the contact force $(-p_m^n\mathbf{n}_m, -p_m^\tau\boldsymbol{\tau}_m)$ applies to vertex V_m of block B_i. We consider a block B_i with n_i contact pairs.

The Newmark scheme[63] with adopted parameters $\gamma = 1.0$ and $\beta = 0.5$ is employed in the time integration of this study. In consideration of the interpolation shape function $\mathbf{T}(x, y)$ and the minimization of total potential energy of the block, the governing equation for a body motion can be expressed as[56]

$$\mathbf{K}_i\mathbf{d}_i - \mathbf{C}_i\mathbf{p}_i = \mathbf{f}_i, \tag{8}$$

where $\mathbf{K}_i$ is the equivalent stiffness matrix, $\mathbf{d}_i$ is the basic unknown vector, and $\mathbf{f}_i$ is the equivalent loading vector. $\mathbf{C}_i$ and $\mathbf{p}_i$ are the contact matrix and the undetermined contact force vector acting on block B_i, respectively. Note that the dimensions of Equation (8) can be 3, 4, or 6 for the rigid particle or block, the deformable particle, or the deformable block, respectively. For a rigid or deformable particle, the Appendix summarizes the analysis formulas of key submatrices needed for the generation of $\mathbf{K}_i$; while for a rigid or deformable block, the simplex integration method[52] is adopted.

The contact matrix is given by

$$\mathbf{C}_i = \left[\mathbf{C}_i^1, \mathbf{C}_i^2, \ldots, \mathbf{C}_i^k, \ldots, \mathbf{C}_i^{n_i}\right], \tag{9}$$

where each $\mathbf{C}_i^k$ is the 3×2, 4×2, or 6×2 matrix associated with the kth contact pair on block B_i defined as follows:

$$\mathbf{C}_i^k(x_k, y_k) = s_k\mathbf{T}_i^{\mathrm{T}}(x_k, y_k)[\mathbf{n}_k, \boldsymbol{\tau}_k], \qquad k = 1, \ldots, n_i, \tag{10}$$

where (x_k, y_k) are the coordinates of the kth contact point and s_k is the sign indicating that the kth contact force is either positive or negative according to the definition of the unit normal and shear vector. In addition, the 2×2 matrix $[\mathbf{n}_k, \boldsymbol{\tau}_k]$ is expressed as

$$[\mathbf{n}_k, \boldsymbol{\tau}_k] = \begin{bmatrix} \cos\alpha_k^n & \cos\alpha_k^\tau \\ \cos\beta_k^n & \cos\beta_k^\tau \end{bmatrix}, \tag{11}$$

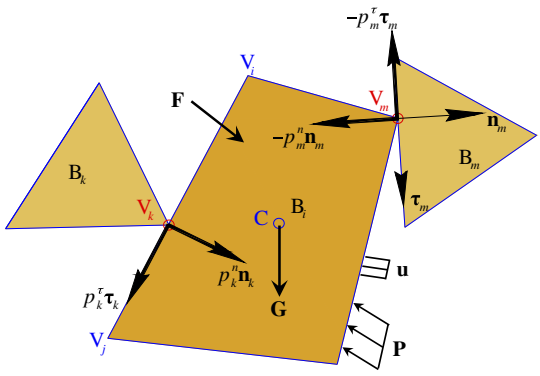

FIGURE 8 Edge-edge contacts of the block-block contact [Colour figure can be viewed at wileyonlinelibrary.com]

where $(\cos\alpha_k^n, \cos\beta_k^n)$ and $(\cos\alpha_k^\tau, \cos\beta_k^\tau)$ are the direction cosines of the vectors $\mathbf{n}_k$ and $\boldsymbol{\tau}_k$, respectively. The contact force vector $\mathbf{p}_i$ for the n_i contact pairs on block B_i is

$$\mathbf{p}_i = \left[p_1^n, p_1^\tau, p_2^n, p_2^\tau, \ \cdots\ , p_{n_i}^n, p_{n_i}^\tau\right]^{\mathrm{T}}. \tag{12}$$

If the action point of a point loading does not coincide with the centroid of a body, the point loading may result in both body translation and rotation. For a rigid body, the following interpolation shape function can be used to translate the point load into an equivalent loading vector:

$$\mathbf{T}^{\mathrm{R}}(x, y) = \begin{bmatrix} 0 & 0 & y_c - y \\ 0 & 0 & x - x_c \end{bmatrix}, \tag{13}$$

such that the point loading will only cause the rotation of the rigid body. As illustrated in Figure 9, the use of $\mathbf{T}^{\mathrm{R}}(x, y)$ renders the effect of loading $\mathbf{F}$ applied at point $A(x, y)$ to be equivalent to the moment $\mathbf{m}^{\mathrm{R}}$ acting on the centroid $C(x_c, y_c)$. Indeed, $\mathbf{T}^{\mathrm{R}}(x, y)$ will also be employed in the implementation of the rolling resistance.

Note that, for a deformable particle, $\mathbf{T}^{\mathrm{R}}(x, y)$ becomes

$$\mathbf{T}^{\mathrm{R}}(x, y) = \begin{bmatrix} 0 & 0 & y_c - y & x - x_c \\ 0 & 0 & x - x_c & y - y_c \end{bmatrix}, \tag{14}$$

while for a deformable block, $\mathbf{T}^{\mathrm{R}}(x, y)$ should be written as

$$\mathbf{T}^{\mathrm{R}}(x, y) = \begin{bmatrix} 0 & 0 & y_{\mathrm{c}} - y & x - x_{\mathrm{c}} & 0 & \frac{y - y_{\mathrm{c}}}{2} \\ 0 & 0 & x - x_{\mathrm{c}} & 0 & y - y_{\mathrm{c}} & \frac{x - x_{\mathrm{c}}}{2} \end{bmatrix}. \tag{15}$$

It should be noted that the interpolation shape function $\mathbf{T}(x, y)$ or $\mathbf{T}^{\mathrm{R}}(x, y)$ and the basic unknown vector $\mathbf{d}$ are only used to construct the governing equation. To overcome the possible volume expansion caused by the rotation of rigid body, the postadjusted method will be employed to calculate the displacement of any point after solving the controlling equation. For a rigid particle or block, the postadjusted displacements are[55]

$$\begin{cases} u_x = u_0 + (x - x_{\mathrm{c}})(\cos\theta - 1) - (y - y_{\mathrm{c}})\sin\theta \\ u_y = v_0 + (x - x_{\mathrm{c}})\sin\theta + (y - y_{\mathrm{c}})(\cos\theta - 1), \end{cases} \tag{16}$$

while for a deformable particle,

$$\begin{cases} u_x = u_0 + (x - x_{\mathrm{c}})(\cos\theta - 1) - (y - y_{\mathrm{c}})\sin\theta + (x - x_{\mathrm{c}})\varepsilon \\ u_y = v_0 + (x - x_{\mathrm{c}})\sin\theta + (y - y_{\mathrm{c}})(\cos\theta - 1) + (y - y_{\mathrm{c}})\varepsilon, \end{cases} \tag{17}$$

and for the deformable block,[34]

$$\begin{cases} u_x = u_0 + (x - x_{\mathrm{c}})(\cos\theta - 1) - (y - y_{\mathrm{c}})\sin\theta + (x - x_{\mathrm{c}})\varepsilon_x + (y - y_{\mathrm{c}})\gamma_{xy}/2 \\ u_y = v_0 + (x - x_{\mathrm{c}})\sin\theta + (y - y_{\mathrm{c}})(\cos\theta - 1) + (y - y_{\mathrm{c}})\varepsilon_y + (x - x_{\mathrm{c}})\gamma_{xy}/2. \end{cases} \tag{18}$$

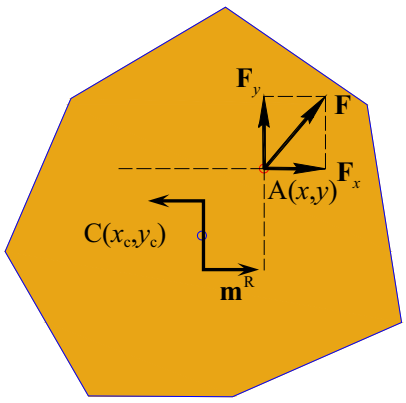

FIGURE 9 Equivalent moment caused by a point loading [Colour figure can be viewed at wileyonlinelibrary.com]

4.2 | Contact force

Frictional resistance will be triggered when there is either a trend of relative sliding or a real relative sliding occurring along the contact surface defined previously, according to the static friction and the sliding friction, respectively. For a typical vertex-edge contact pair k, if the following shear strength is adopted:

$$\tau\left(p_k^n\right) = c_k + \mu_k p_k^n, \tag{19}$$

where p_k^n is the normal contact force of the kth contact pair, c_k is the cohesion of the contact surface, and μ_k is the sliding friction coefficient. Equation (19) is a function of p_k^n. Considering the Coulomb friction law, the friction-induced shear contact force p_k^τ should fall in the interval of $[-\tau(p_k^n), \tau(p_k^n)]$. In other words, the shear contact force p_k^τ is a function of the normal contact force p_k^n. On the other hand, because the contact force vector $\mathbf{p}_i$ in Equation (8) is undetermined, in order to obtain the basic unknown vector $\mathbf{d}_i$ in Equation (8), $\mathbf{d}_i$ can be split into the following 2 components:

$$\mathbf{d}_i = \mathbf{d}_i^p + \mathbf{d}_i^f, \tag{20}$$

where $\mathbf{d}_i^p$ and $\mathbf{d}_i^f$ are the contributions of the contact force vector $\mathbf{p}_i$ and the equivalent loading vector $\mathbf{f}_i$, respectively. As a result, Equation (8) can be further rewritten as

$$\mathbf{K}_i\mathbf{d}_i^f = \mathbf{f}_i, \tag{21}$$

and

$$\mathbf{K}_i\mathbf{d}_i^p = \mathbf{C}_i\mathbf{p}_i. \tag{22}$$

Indeed, the partition expressed by Equation (20) embodies the idea of "predictor-corrector" technique as follows. A "predicted value" is first obtained without considering the contact force, and a "corrected value" is then calculated when the contact force is considered, which is further added to the "predicted value." As a matter of convenience, Equations (21) and (22) are referred to as "noncontact step" and "contact step," respectively. From Equations (21) and (22), we can readily calculate

$$\mathbf{d}_i^f = \mathbf{K}_i^{-1}\mathbf{f}_i, \tag{23}$$

$$\mathbf{d}_i^p = \mathbf{K}_i^{-1}\mathbf{C}_i\mathbf{p}_i. \tag{24}$$

To determine $\mathbf{d}_i^p$, one needs to solve the contact force vector $\mathbf{p}_i$ first. According to the work of Zheng et al,[56] the constraints of no-penetration constraint and no-tension constraint at the contact point can be translated into the following complementarity condition:

$$\begin{cases} g_k^n \geq 0,\ p_k^n \geq 0 \\ g_k^n p_k^n = 0, \end{cases} \tag{25}$$

which is equivalent to the variational inequality VI-$p^n(k)$. Find $p_k^n \geq 0$ such that

$$\left(q_k^n - p_k^n\right) g_k^n \geq 0, \quad \forall q_k^n \geq 0, \tag{26}$$

where q_k^n is related to the normal contact force p_k^n and g_k^n is the normal contact gap of the kth contact pair. Moreover, the Coulomb friction law can be reformulated into the following condition:

$$g_k^\tau \begin{cases} \geq 0, & \text{if } p_k^\tau = -\tau\left(p_k^n\right) \\ = 0, & \text{if } \left|p_k^\tau\right| < \tau\left(p_k^n\right) \\ \leq 0, & \text{if } p_k^\tau = \tau\left(p_k^n\right), \end{cases} \tag{27}$$

where g_k^τ is the tangential relative sliding gap of the kth contact pair and $\tau(p_k^n)$ is determined by Equation (19). Furthermore, the condition Equation (27) is equivalent to the quasivariational inequality QVI-$p^\tau(k)$. Find $|p_k^\tau| \leq \tau(p_k^n)$ such that

$$\left(q_k^\tau - p_k^\tau\right) g_k^\tau \geq 0, \quad \forall \left|q_k^\tau\right| \leq \tau\left(p_k^n\right). \tag{28}$$

In the following, we will redefine the gaps g_k^n and g_k^τ. For a typical kth vertex-edge contact pair shown in Figure 10, at the starting time t_0 of the current time step, the contact point $\mathrm{V}_k^i(x_i^0, y_i^0)$ belonging to block B_i coincides with the contact point $\mathrm{V}_k^j(x_j^0, y_j^0)$ that belongs to block B_j. At the end of the time step $t_0 + \Delta t$, the contact points V_k^i and V_k^j move to $\mathrm{V}_k^{i^*}(x_i, y_i)$

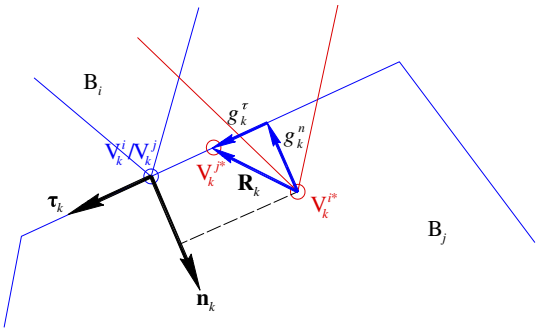

FIGURE 10 One pair of vertex-edge contacts [Colour figure can be viewed at wileyonlinelibrary.com]

and $\mathrm{V}_k^{j^*}(x_j, y_j)$, respectively. The normal contact gap g_k^n is the projection of the vector $\mathbf{R}_k$ pointing $\mathrm{C}_k^{i^*}$ to $\mathrm{C}_k^{j^*}$ onto $\mathbf{n}_k$, according to

$$g_k^n = \mathbf{n}_k^{\mathrm{T}}(\mathbf{x}_j - \mathbf{x}_i), \tag{29}$$

where

$$\mathbf{x}_m = [x_m, y_m]^{\mathrm{T}} = \left[x_m^0, y_m^0\right]^{\mathrm{T}} + \mathbf{T}_m\left(x_m^0, y_m^0\right)\left(\mathbf{d}_m^f + \mathbf{d}_m^p\right), \quad m = i, j. \tag{30}$$

After some mathematical manipulations, we have

$$g_k^n = p_{ij}^n + g_{ij}^n, \tag{31}$$

where

$$\begin{aligned} p_{ij}^n &= \mathbf{n}_{ki}^{\mathrm{T}}\mathbf{p}_i - \mathbf{n}_{kj}^{\mathrm{T}}\mathbf{p}_j \\ \mathbf{n}_{ki}^{\mathrm{T}} &= \mathbf{n}_k^{\mathrm{T}}\mathbf{T}_i\tilde{\mathbf{F}}_i \\ \mathbf{n}_{kj}^{\mathrm{T}} &= \mathbf{n}_k^{\mathrm{T}}\mathbf{T}_j\tilde{\mathbf{F}}_j, \end{aligned} \tag{32}$$

and

$$\tilde{\mathbf{F}}_m = \mathbf{K}_m^{-1}\mathbf{C}_m, \quad m = i, j, \tag{33}$$

$$g_{ij}^n = \mathbf{n}_k^{\mathrm{T}}\left(\mathbf{x}_j^0 - \mathbf{x}_i^0 + \mathbf{T}_j\mathbf{d}_j^f - \mathbf{T}_i\mathbf{d}_i^f\right), \tag{34}$$

where $\mathbf{C}_m(m = i,\ j)$ is the contact matrix (Equation (9)). Note that $\mathbf{x}_j^0 - \mathbf{x}_i^0 = \mathbf{0}$ at the start of the current time step; Equation (34) is reduced to

$$g_{ij}^n = \mathbf{n}_k^{\mathrm{T}}\left(\mathbf{T}_j\mathbf{d}_j^f - \mathbf{T}_i\mathbf{d}_i^f\right). \tag{35}$$

In the tangential direction, the tangential relative sliding gap g_k^τ is defined as

$$g_k^\tau = \boldsymbol{\tau}_k^{\mathrm{T}}(\mathbf{u}_j - \mathbf{u}_i), \tag{36}$$

where

$$\mathbf{u}_m = \left[u_m^x,\ u_m^y\right]^{\mathrm{T}} = \mathbf{T}_m\left(x_m^0,\ y_m^0\right)\left(\mathbf{d}_m^f + \mathbf{d}_m^p\right), \quad m = i, j. \tag{37}$$

Similar to g_k^n, we have

$$\begin{aligned} p_{ij}^\tau &= \boldsymbol{\tau}_{ki}^{\mathrm{T}}\mathbf{p}_i - \boldsymbol{\tau}_{kj}^{\mathrm{T}}\mathbf{p}_j \\ \boldsymbol{\tau}_{ki}^{\mathrm{T}} &= \boldsymbol{\tau}_k^{\mathrm{T}}\mathbf{T}_i\tilde{\mathbf{F}}_i \\ \boldsymbol{\tau}_{kj}^{\mathrm{T}} &= \boldsymbol{\tau}_k^{\mathrm{T}}\mathbf{T}_j\tilde{\mathbf{F}}_j \\ g_{ij}^\tau &= \boldsymbol{\tau}_k^{\mathrm{T}}\left(\mathbf{T}_j\mathbf{d}_j^f - \mathbf{T}_i\mathbf{d}_i^f\right). \end{aligned} \tag{38}$$

Since the contact points V_k^i and V_k^j are at the same location at the start of the current time step, g_k^τ is exactly the projection of the vector $\mathbf{R}_k$ onto $\boldsymbol{\tau}_k$. Moreover, g_k^n and g_k^τ are all functions of the contact force vectors $\mathbf{p}_i$ and $\mathbf{p}_j$. Hereafter, $\tilde{\mathbf{F}}$ is called the flexibility matrix.

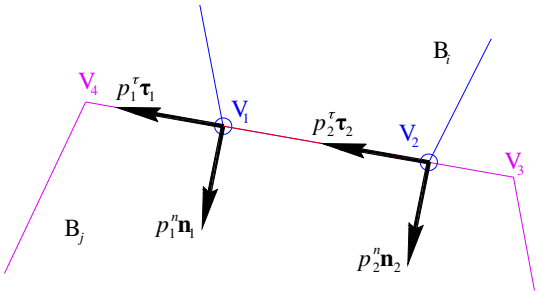

FIGURE 11 Two pairs of adjoint vertex-edge contacts [Colour figure can be viewed at wileyonlinelibrary.com]

If there are N contact pairs in a discrete particle-block system at the current time step, each contact pair corresponds to the variational inequality VI-p^n and the quasivariational inequality QVI-p^τ. By combining all of these VI-p^n and QVI-p^τ, we have the following dual form of DDA, abbreviated as DDA-d.[56] Find the global contact force vector $\mathbf{p} \in X(\mathbf{p}) \subset R^{2N}$ such that

$$(\mathbf{q}-\mathbf{p})^{\mathrm{T}}\mathbf{G}(\mathbf{p}) \geq 0, \quad \forall \mathbf{q} \in X(\mathbf{p}), \tag{39}$$

where

$$\mathbf{p} = \left[p_1^n, p_1^\tau, \ \cdots, p_N^n, p_N^\tau\right]^{\mathrm{T}}, \tag{40}$$

and the constraint $X(\mathbf{p})$ is a closed set in R^{2N} and dependents on the global contact force vector $\mathbf{p}$. In addition, the contact gap function $\mathbf{G}(\mathbf{p})$ is defined as

$$\mathbf{G}(\mathbf{p}) = \left[g_1^n(\mathbf{p}), g_1^\tau(\mathbf{p}), \ \cdots, g_N^n(\mathbf{p}), g_N^\tau(\mathbf{p})\right]^{\mathrm{T}}. \tag{41}$$

One can refer to the work of Zheng et al[56] for more detail. In this study, the compatibility iteration[56] based on the projection-contraction algorithm[64] will be adopted, which, in conjunction with the variational or quasivariational inequality formulations, can help totally avoid using the artificial contact spring, and may replace the OCI of the original DDA to solve all the contact forces occurring in a discrete particle-block system.

In addition, note that the shear strength described by Equation (19) is no longer suitable for the adjoint vertex-edge contact, which stems from a same edge-edge contact when the cohesion c is nonzero. The shear strength for the adjoint vertex-edge contact needs to be reexamined specifically. As shown in Figure 11, vertex-edge contacts V_1-$V_3V_{4\text{-BB}}$ and V_2-$V_3V_{4\text{-BB}}$ are 2 adjoint vertex-edge contact pairs, which should join together to resist the potential tangential sliding. It has been reported that there is an unreasonable sharing ratio[65] between them in the OCI of the original DDA. This unreasonable ratio may cause that the 2 contact pairs cannot undergo the state of opening, sliding, or closing at the same time. If the cohesion $c \neq 0$, we might rewrite c as follows:

$$c = c_1 + c_2, \tag{42}$$

where c_1 and c_2 correspond to the contributions by contacts V_1-$V_3V_{4\text{-BB}}$ and V_2-$V_3V_{4\text{-BB}}$, respectively, and satisfy

$$k_{\mathrm{c}} = \frac{c_1}{c_2} = 1, \tag{43}$$

and thus, for the contact V_1-$V_3V_{4\text{-BB}}$, the shear strength can be given by

$$\tau\left(p_1^n\right) = \frac{k_{\mathrm{c}}}{1+k_{\mathrm{c}}}c + \mu_1 p_1^n, \tag{44}$$

and for the contact V_2-$V_3V_{4\text{-BB}}$, the shear strength reads

$$\tau\left(p_2^n\right) = \frac{1}{1+k_{\mathrm{c}}}c + \mu_2 p_2^n. \tag{45}$$

At the end of the compatibility iteration,[56] k_c will converge to an appropriate value, leading naturally to a final unique compatible contact state for the 2 adjoint vertex-edge contact pairs.

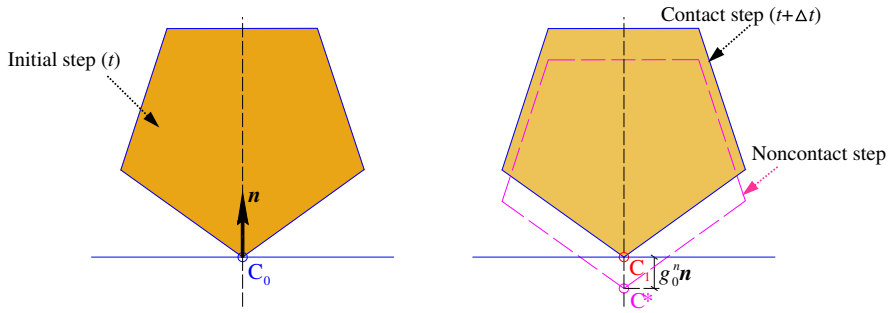

FIGURE 12 Illustration of unphysical "one-step lag" [Colour figure can be viewed at wileyonlinelibrary.com]

4.3 | One-step lag

Once the compatibility iteration is completed, the contact conditions of no penetration and no tension at the contact points are expected to be satisfied. More specifically, the normal gaps should all be equal to zero, and the shear gaps converge to correct values. However, according to our numerical experience, there are cases where an unphysical phenomenon of "one-step lag" may occur in the aforementioned "predictor-corrector" process, which needs to be fixed. To demonstrate this, the normal contact, as shown in Figure 12, is taken as an example.

Assume that there is a contact pair at the initial step (at time t), with point C_0 being the contact point (see Figure 12). During the noncontact step, namely, when the contact force is not considered, contact point C_0 reaches at point C*, leading to an initial nonzero normal contact gap $g_0^n\mathbf{n} \neq \mathbf{0}$. The compatibility iteration is then invoked until the convergence is achieved to determine the normal contact force. The determined contact force is further considered to carry out the contact step in an attempt to make $g_0^n\mathbf{n} = \mathbf{0}$, equivalently, to push point C* back to point C_1 at time $t + \Delta t$. Now, the following phenomenon can be clearly pictured. After the time interval Δt, the position of the contact point remains at its initial position. Physically, the normal contact force should occur at the time when contact occurs, but the normal contact gap does not yet appear. In addition, the same applies to the shear direction. This phenomenon is the so-called "one-step lag". If the initial velocity component of any block or particle is not equal to zero at the initial time t, to eliminate this undesired lag, the ultimate basic known at time $t + \Delta t$ is estimated by

$$if\left(v_i^0 \neq 0\right) \quad \bar{\bar{d}}_i = 2d_i^p + d_i^f, \quad (i = 1, 2, \ldots, k), \tag{46}$$

where k is equal to 3 for rigid body or 4 for deformable particle or 6 for deformable block. This is to say that the displacement caused by the contact force is doubled at $t + \Delta t$ time. Equation (46) is referred to as "double contact displacement" in this paper.

In the Newmark time integration, the velocity and acceleration are computed based on the basic knowns. Thus, the modified basic known $\bar{\bar{\mathbf{d}}}$ (see Equation (46)) can be used to update the stress and the relevant geometry, while the original basic known $\mathbf{d}$ (see Equation (20)) is still employed to calculate the velocity and acceleration. This is demonstrated in the following examples.

4.4 | Rolling resistance for particles

Rolling resistance may become important for a particle-particle contact or a particle-block contact. An illustration of modeling of rolling resistance in this study is shown in Figure 13. There is a contact pair between particle O_i(the centroid of the particle) and surface AB. Vectors $\mathbf{n}$ and $\boldsymbol{\tau}$ are the unit normal and shear vector, respectively. $\mathbf{G}$ is the gravity force of the particle, and $\mathbf{F}$ is the point loading acting on point A. While $p^n\mathbf{n}$ is the normal contact force determined by the compatibility iteration, $\widehat{p}^{\,\tau}\boldsymbol{\tau}$ can is called the unknown rolling friction. ω_0 is the initial angle velocity, d^{R} is an undetermined distance, and δ is the rolling friction coefficient with a dimension of length.

The rolling resistance is intended both to limit the translational motion of the particle and to suppress its rotation. To this end, we consider the contact point C as a temporary fixed point inspired by the fact that the contact point C is the instantaneous center of rotation, which implies that the instantaneous velocity of point C is zero. We then move the normal contact force $p^n\mathbf{n}$ by an undetermined distance d^{R} on the contact surface AB; thus, we have a normal rolling resistance force $\widehat{p}^{\,n}\mathbf{n}$, as shown in Figure 13. An equivalent moment, referred to as the rolling resistance moment, can

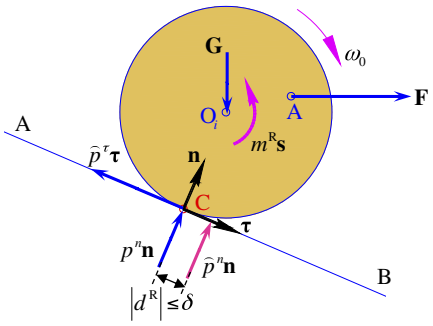

FIGURE 13 Modeling of rolling resistance for particles [Colour figure can be viewed at wileyonlinelibrary.com]

then be constructed as follows:

$$\begin{aligned} m^R\mathbf{s} &= \widehat{p}^{\,n}\mathbf{n}\times d^R\boldsymbol{\tau} \\ \mathbf{s} &= \mathbf{n}\times\boldsymbol{\tau}. \end{aligned} \tag{47}$$

Suppose that there are n_R rolling resistant forces acting on the particle O_i, by applying the interpolation shape function $\mathbf{T}^R(x, y)$ expressed by Equation (13), (14), or (15), the total applied moment $m^R\mathbf{s}$ can be translated into the equivalent loading vector for the governing equation

$$\mathbf{R}_i\mathbf{m}_i^R \to \mathbf{f}_i, \tag{48}$$

where

$$\mathbf{m}_i^R = \left[m_1^R\mathbf{s}_1, \ldots, m_{n_R}^R\mathbf{s}_{n_R}\right]^T = \left[\widehat{p}_1^{\,n}\mathbf{n}_1\times d_1^R\boldsymbol{\tau}_1, \ldots, \widehat{p}_{n_R}^{\,n}\mathbf{n}_{n_R}\times d_{n_R}^R\boldsymbol{\tau}_{n_R}\right]^T, \tag{49}$$

which is referred to as the rolling resistance moment vector, and

$$\mathbf{R}_i = \left[\mathbf{T}_1^R, \ldots, \mathbf{T}_{n_R}^R\right]. \tag{50}$$

The matrix $\mathbf{R}_i$ is called the rolling resistance matrix in this study. The exerted moment $m^R\mathbf{s}$ on the particle may lead to an additional contribution to the basic unknown vector as follows:

$$\mathbf{d}_i^R \to \mathbf{d}_i, \tag{51}$$

where $\mathbf{d}_i^R$ is caused by the rolling resistance moment $\mathbf{m}_i^R$. Since point C is assumed to be temporarily fixed, the displacement $\mathbf{u}_O = (u_{ox}, u_{oy})^T$ of point O is maybe nonzero. According to Newton's second law, one has

$$\widehat{p}^{\,\tau} = \frac{2M_{ass}\widehat{d}^{\,\tau}}{(\Delta t)^2}, \tag{52}$$

where M_{ass} is the mass of the particle, Δt is the time step size, and $\widehat{d}^{\,\tau}$ is the tangential displacement of point O given by

$$\widehat{d}^{\,\tau} = \mathbf{u}_O^T\boldsymbol{\tau}. \tag{53}$$

In practice, there is no need to consider the force $\widehat{p}^{\,\tau}$ since its action point C has been temporarily fixed.

For an arbitrary kth rolling resistance, due to the moment $m^R\mathbf{s}$, the particle undergoes a rotation angle θ_m. Considering the initial angle velocity ω_0 and the rotation angle θ_f caused by external loads, we have the following total rotation angle:

$$g_k^R\left(m_k^R\mathbf{s}\right) = \omega_0\Delta t + \theta_f + \theta_m. \tag{54}$$

In this study, g_k^R is called the rolling gap, taking counterclockwise as positive. In analogy to the shear strength, a "rolling strength" is defined as follows:

$$\tau^R\left(d_k^R\right) = \widehat{p}_k^{\,n}d_k^R, \tag{55}$$

where d_k^R (see Figure 13) is undetermined. In analogy to the Coulomb friction law, one can have the following condition similar to Equation (27):

$$g_k^R\begin{cases} \ge 0, & \text{if } m_k^R = -\tau^R\left(d_k^R\right) \\ = 0, & \text{if } \left|m_k^R\right| < \tau^R\left(d_k^R\right) \\ \le 0, & \text{if } m_k^R = \tau^R\left(d_k^R\right). \end{cases} \tag{56}$$

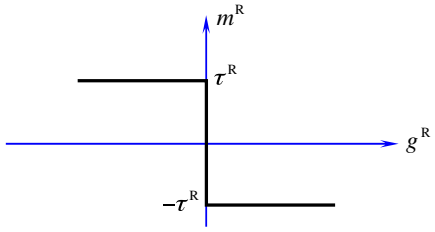

FIGURE 14 Relationship between the rolling gap g^{R} and the rolling resistance moment m^{R} [Colour figure can be viewed at wileyonlinelibrary.com]

Indeed, g_k^{R} and m_k^{R} can be seen as a pair complementary variable. Figure 14 depicts the relationship between them.

Consequently, we can further establish the following equivalent quasivariational inequality QVI-$m^{\mathrm{R}}(k)$. Find $|m_k^{\mathrm{R}}| \leq \tau^{\mathrm{R}}(d_k^{\mathrm{R}})$ such that

$$\left(q_k^{\mathrm{R}} - m_k^{\mathrm{R}}\right) g_k^{\mathrm{R}} \geq 0, \qquad \forall \left|q_k^{\mathrm{R}}\right| \leq \tau^{\mathrm{R}}\left(d_k^{\mathrm{R}}\right), \tag{57}$$

which is a counterpart to Equation (28) in the rolling case.

If there are N rolling resistances in the discrete particle-block system at the current time step, there are N quasivariational inequalities QVI-m^{R}. Assembling them leads to the following formulation for the rolling resistance.
Find the global rolling resistance moment vector $\mathbf{M}^{\mathrm{R}} \in X(\mathbf{M}^{\mathrm{R}}) \subset R^N$ such that

$$\left(\mathbf{q}^{\mathrm{R}} - \mathbf{M}^{\mathrm{R}}\right)^{\mathrm{T}} \mathbf{G}(\mathbf{M}^{\mathrm{R}}) \geq 0, \quad \forall \mathbf{q}^{\mathrm{R}} \in X(\mathbf{M}^{\mathrm{R}}), \tag{58}$$

where

$$\mathbf{M}^{\mathrm{R}} = \left[m_1^{\mathrm{R}}, m_2^{\mathrm{R}}, \ldots, m_N^{\mathrm{R}}\right]^{\mathrm{T}}, \tag{59}$$

and the rolling gap function $\mathbf{G}(\mathbf{M}^{\mathbf{R}})$ reads

$$\mathbf{G}(\mathbf{M}^{\mathrm{R}}) = \left[g_1^{\mathrm{R}}(\mathbf{M}^{\mathrm{R}}), \ldots, g_k^{\mathrm{R}}(\mathbf{M}^{\mathrm{R}}), \ldots, g_N^{\mathrm{R}}(\mathbf{M}^{\mathrm{R}})\right]^{\mathrm{T}}, \tag{60}$$

where the rolling gap $g_k^{\mathrm{R}}(\mathbf{M}^{\mathrm{R}})$ is defined by Equation (54). Moreover, the constraint $X(\mathbf{M}^{\mathrm{R}})$ is dependent on the $\mathbf{M}^{\mathrm{R}}$ and is a closed set in R^N as follows:

$$X(\mathbf{M}^{\mathrm{R}}) = X_1\left(m_1^{\mathrm{R}}\right) \times \cdots \times X_k\left(m_k^{\mathrm{R}}\right) \times \cdots \times X_N\left(m_N^{\mathrm{R}}\right), \tag{61}$$

where $X_k(\mathbf{m}_k^{\mathrm{R}}) \subset R$ is the constraint set of the rolling resistance moment m_k^{R} in the kth rolling resistance and relies on the distance d_k^{R} associated with the kth rolling resistance. It is given by

$$X_k\left(m_k^{\mathrm{R}}\right) = \left\{ \left|m_k^{\mathrm{R}}\right| \leq \tau^{\mathrm{R}}\left(d_k^{\mathrm{R}}\right) \right\} = \left[-\tau^{\mathrm{R}}\left(d_k^{\mathrm{R}}\right), \tau^{\mathrm{R}}\left(d_k^{\mathrm{R}}\right)\right], \tag{62}$$

for $k = 1, \ldots, N$, with $\tau^{\mathrm{R}}(d_k^{\mathrm{R}})$ defined by Equation (55).

4.5 | Tensile resistance at cemented interface

Cementations may exist at natural or artificial interfaces or joints and may account for certain tensile strength at the interface or joint. Take the case in Figure 15 as example. Two blocks, connected by a joint k, are subjected to 3 forces $\mathbf{F}_1$, $\mathbf{F}_2$, and $\mathbf{F}_3$ acting on points A_1, A_2, and A_3, respectively. The tensile resistance offered by the joint $\mathrm{C}_k^i/\mathrm{C}_k^j$ is in an opposite direction to the interface tension $-p_k^{\mathrm{t}}\mathbf{n}_k$ and acting on point C_k^i of block B_i, where the definition of $\mathbf{n}_k$ is the same as Section 3. Assume that the allowable tensile deformation of the cementing material is d_0^{t}. In other words, the interface tension $-p_k^{\mathrm{t}}\mathbf{n}_k$ will reach its maximum once the distance $\bar{g}_k^{\mathrm{t}}$ between points C_k^i and C_k^j is equal to d_0^{t}. Moreover, if the distance continues to be increased, the cementing material will be broken. According to

$$g_k^{\mathrm{t}} = \bar{g}_k^{\mathrm{t}} - d_0^{\mathrm{t}} \begin{cases} > 0, & \text{if } p_k^{\mathrm{t}} = 0 \\ = 0, & \text{if } 0 \leq p_k^{\mathrm{t}} \leq t_k, \end{cases} \tag{63}$$

where t_k is the tensile strength of joint k and g_k^{t} is called the tensile gap. In this study, 4 hypotheses are adopted. (i) Only the cemented joints or interfaces detected at time $t = 0$ is needed to be considered. (ii) The cementing material is inextensible before failure, namely, $d_0^{\mathrm{t}} = 0$, as illustrated in Figure 16. (iii) The external force does not effect on the tensile strength of cementing material before failure. (iv) The tensile strength of cementing material is unrecoverable after failure.

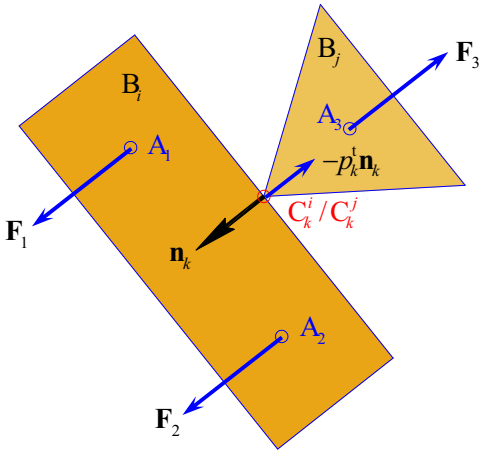

FIGURE 15 Tensile strength at joint between 2 blocks [Colour figure can be viewed at wileyonlinelibrary.com]

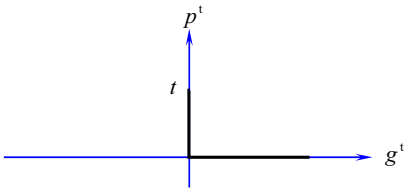

FIGURE 16 Relationship between tensile gap g^t and interface tension p^t [Colour figure can be viewed at wileyonlinelibrary.com]

Furthermore, Equation (63) can be made equivalent to its variational inequality VI-$p^t(k)$. Find $0 \le p_k^t \le t_k$ such that

$$\left(q_k^t - p_k^t\right) g_k^t \ge 0, \quad \forall 0 \le q_k^t \le t_k. \tag{64}$$

If there are N joints in the discrete particle-block system at the current time step, there will be N variational inequalities VI-p^t, which combine to form the following variational formulation for the tensile resistance at the interface.

Find the global interface tension vector $\mathbf{p}^t \in X(\mathbf{p}^t) \subset R^N$ such that

$$(\mathbf{q}^t - \mathbf{p}^t)^t \mathbf{G}(\mathbf{p}^t) \ge 0, \quad \forall \mathbf{q}^t \in X(\mathbf{p}^t), \tag{65}$$

where

$$\mathbf{p}^t = \left[p_1^t, p_2^t, \ldots, p_N^t\right]^T, \tag{66}$$

and the tensile gap function $\mathbf{G}(\mathbf{p}^t)$ is given by

$$\mathbf{G}(\mathbf{p}^t) = \left[g_1^t(\mathbf{p}^t), \ldots, g_k^t(\mathbf{p}^t), \ldots, g_N^t(\mathbf{p}^t)\right]^T, \tag{67}$$

where $g_k^t(\mathbf{p}^t) \le$ is the tensile gap. In addition, the constraint $X(\mathbf{p}^t)$ depending on the $\mathbf{p}^t$ is a closed set in R^N and is defined by

$$X(\mathbf{p}^t) = X_1(p_1^t) \times \cdots \times X_k(p_k^t) \times \cdots \times X_N(p_N^t), \tag{68}$$

where $X_k(p_k^t) \subset R$ is the constraint set of the interface tension p_k^t corresponding to the kth joints defined by

$$X_k\left(p_k^t\right) = \left\{0 \le p_k^t \le t_k\right\} = [0, \ t_k], \tag{69}$$

for $k = 1, \ldots, N$.

Similar case may exist at the interface between 2 blocks, as shown in Figure 17. Suppose 2 forces $\mathbf{F}_1$ and $\mathbf{F}_2$ are applied to the 2 blocks at points A_1 and A_2, respectively. The tensile resistance exerted by the cemented interface $C_1^i C_2^i$ may be transferred to the 2 joints C_1^i and C_2^i. Namely, the tensile resistance is in opposite direction to the resultant force of the interface tensions $-p_1^t \mathbf{n}_1$ and $-p_2^t \mathbf{n}_2$ acting on points C_1^i and C_2^i of block B_i, respectively. We assume an additive tensile strength

$$t = t_1 + t_2, \tag{70}$$

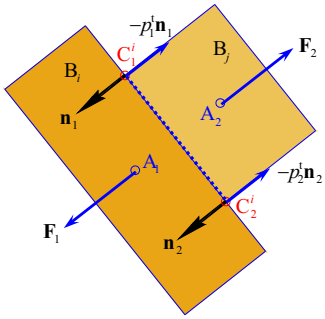

FIGURE 17 Tensile resistance at interface between 2 blocks [Colour figure can be viewed at wileyonlinelibrary.com]

where t_1 and t_2 correspond to contributions by joints C_1^i and C_2^i, respectively. A tensile-shearing ratio between the two is introduced

$$k_t = \frac{t_1}{t_2} = \frac{|p_1^t|}{|p_2^t|}, \tag{71}$$

to facilitate their individual contribution can be appropriately specified. The 2 joints, ie, C_1^i and C_2^i, which belong to the same cementing interface, are called "adjoint joints" in this study. Hence, for a pair of adjoint joints, the condition in Equation (63) becomes

$$\begin{cases} g_1^t = \bar{g}_1^t - d_0^t \begin{cases} > 0, & \text{if } p_1^t = 0 \\ = 0, & \text{if } 0 \le p_1^t \le t_1 \end{cases} \\ g_2^t = \bar{g}_2^t - d_0^t \begin{cases} > 0, & \text{if } p_2^t = 0 \\ = 0, & \text{if } 0 \le p_2^t \le \quad t_2, \end{cases} \end{cases} \tag{72}$$

where

$$t_1 = \frac{k_t}{1+k_t}t, \qquad t_2 = \frac{1}{1+k_t}t. \tag{73}$$

5 | CONNECTOR

In a discrete particle/block system, any 2 independent particles or blocks can be connected through one or more connectors. The connectors considered in this study include rock bolts, springs, and beams.

5.1 | Rock bolt connector

The rock bolt is an effective reinforcement in civil and mining engineering. The original DDA is capable of simulating the behavior of rock bolt. Figure 18 shows 2 blocks B_i and B_j connected by a rock bolt A_1A_2, where points $A_1(x_1, y_1)$ and $A_2(x_2, y_2)$ are the 2 connecting points and forces $\mathbf{F}_1$ and $\mathbf{F}_2$ are the 2 axial forces acting on points A_1 and A_2, respectively. According to the original DDA without considering the blot, the governing equation of the 2 blocks can be expressed as

$$\begin{bmatrix} \mathbf{K}_{i,i} & \mathbf{K}_{i,j} \\ \mathbf{K}_{j,i} & \mathbf{K}_{j,j} \end{bmatrix} \begin{bmatrix} \mathbf{d}_i \\ \mathbf{d}_j \end{bmatrix} = \begin{bmatrix} \mathbf{f}_i \\ \mathbf{f}_j \end{bmatrix}$$
$$\mathbf{K}_{i,i} = \mathbf{K}_i, \quad \mathbf{K}_{i,j} = \mathbf{K}_{j,i} = \mathbf{0}, \quad \mathbf{K}_{j,j} = \mathbf{K}_j, \tag{74}$$

where $\mathbf{K}_i$, $\mathbf{K}_j$, $\mathbf{d}_i$, $\mathbf{d}_j$, $\mathbf{f}_i$, and $\mathbf{f}_j$ are the equivalent stiffness matrices, the basic unknown vectors, and the equivalent loading vectors corresponding to blocks B_i and B_j, respectively. Meanwhile, the link element in the theory of FEM[66] presents the following form:

$$\begin{bmatrix} \mathbf{k}_{1,1}^{\text{Le}} & \mathbf{k}_{1,2}^{\text{Le}} \\ \mathbf{k}_{2,1}^{\text{Le}} & \mathbf{k}_{2,2}^{\text{Le}} \end{bmatrix} \begin{bmatrix} \mathbf{u}_1 \\ \mathbf{u}_2 \end{bmatrix} = \begin{bmatrix} \mathbf{F}_1 \\ \mathbf{F}_2 \end{bmatrix}, \tag{75}$$

where $\mathbf{u}_1$ and $\mathbf{u}_2$ are the displacements of points A_1 and A_2, respectively, and

$$\mathbf{k}_{1,1}^{\text{Le}} = \frac{EA}{l}\mathbf{L}, \quad \mathbf{k}_{1,2}^{\text{Le}} = \mathbf{k}_{2,1}^{\text{Le}} = -\frac{EA}{l}\mathbf{L}, \quad \mathbf{k}_{2,2}^{\text{Le}} = \frac{EA}{l}\mathbf{L}, \tag{76}$$

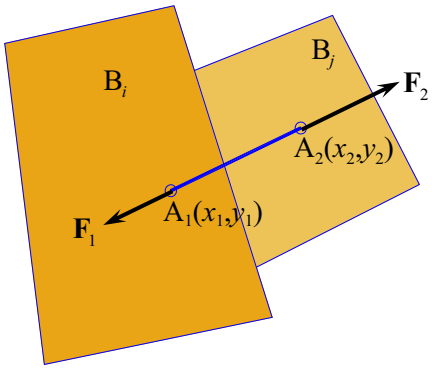

FIGURE 18 Two blocks connected by a rock bolt [Colour figure can be viewed at wileyonlinelibrary.com]

$$\mathbf{L} = \begin{bmatrix} l_x \\ l_y \end{bmatrix} \begin{bmatrix} l_x & l_y \end{bmatrix} = \begin{bmatrix} l_x^2 & l_x l_y \\ l_x l_y & l_y^2 \end{bmatrix}, \tag{77}$$

$$l_x = \frac{x_2 - x_1}{l}, \quad l_y = \frac{y_2 - y_1}{l}, \tag{78}$$

where E, A, and l are Young's modulus, the cross-sectional area, and the length of the link element, respectively. Meanwhile, we have

$$\begin{bmatrix} \mathbf{u}_1 \\ \mathbf{u}_2 \end{bmatrix} = \mathbf{T}_{ij}^{\mathrm{Le}} \begin{bmatrix} \mathbf{d}_i \\ \mathbf{d}_j \end{bmatrix} = \begin{bmatrix} \mathbf{T}_i & 0 \\ 0 & \mathbf{T}_j \end{bmatrix} \begin{bmatrix} \mathbf{d}_i \\ \mathbf{d}_j \end{bmatrix}, \tag{79}$$

where $\mathbf{T}_i$, $\mathbf{T}_j$, $\mathbf{d}_i$, and $\mathbf{d}_j$ are the interpolation shape functions and the basic unknown vectors corresponding to blocks B_i and B_j, respectively.

Substituting Equation (79) into Equation (75) and multiplying it by the transformation matrix $[\mathbf{T}_{ij}^{\mathrm{Le}}]^{\mathrm{T}}$ yields

$$\frac{EA}{l} \mathbf{T}_i^{\mathrm{T}} \begin{bmatrix} l_x \\ l_y \end{bmatrix} \begin{bmatrix} l_x & l_y \end{bmatrix} \mathbf{T}_i \rightarrow \mathbf{K}_{i,i}, \tag{80}$$

$$-\frac{EA}{l} \mathbf{T}_i^{\mathrm{T}} \begin{bmatrix} l_x \\ l_y \end{bmatrix} \begin{bmatrix} l_x & l_y \end{bmatrix} \mathbf{T}_j \rightarrow \mathbf{K}_{i,j}, \tag{81}$$

$$-\frac{EA}{l} \mathbf{T}_j^{\mathrm{T}} \begin{bmatrix} l_x \\ l_y \end{bmatrix} \begin{bmatrix} l_x & l_y \end{bmatrix} \mathbf{T}_i \rightarrow \mathbf{K}_{j,i}, \tag{82}$$

$$\frac{EA}{l} \mathbf{T}_j^{\mathrm{T}} \begin{bmatrix} l_x \\ l_y \end{bmatrix} \begin{bmatrix} l_x & l_y \end{bmatrix} \mathbf{T}_j \rightarrow \mathbf{K}_{j,j}, \tag{83}$$

and

$$\begin{bmatrix} \mathbf{T}_i^{\mathrm{T}} & 0 \\ 0 & \mathbf{T}_j^{\mathrm{T}} \end{bmatrix} \begin{bmatrix} \mathbf{F}_1 \\ \mathbf{F}_2 \end{bmatrix} \rightarrow \begin{bmatrix} \mathbf{f}_i \\ \mathbf{f}_j \end{bmatrix}. \tag{84}$$

By comparison, it is evident that the formulations in Equations (80) to (84) are indeed identical with their counterparts in the original DDA.[31] In other words, because the principle of minimum potential energy is employed by DDA and FEM, we can use the simple transformation matrices and the relevant formulas (Equation (75) for link/bolt element, Equation (85) for spring element, and Equation (87) for beam element) in FEM to establish the controlling equation with considering rock bolt, spring (see Section 5.2), or beam (see Section 5.3).

5.2 | Spring connector

Figure 19 shows 2 blocks B_i and B_j connected by a spring $\mathrm{A}_1\mathrm{A}_2$. Points $\mathrm{A}_1(x_1, y_1)$ and $\mathrm{A}_2(x_2, y_2)$ are the 2 connecting points. Its FEM formula reads

$$\begin{bmatrix} k & -k \\ -k & k \end{bmatrix} \begin{bmatrix} \mathbf{u}_1 \\ \mathbf{u}_2 \end{bmatrix} = \begin{bmatrix} \mathbf{F}_1 \\ \mathbf{F}_2 \end{bmatrix}. \tag{85}$$

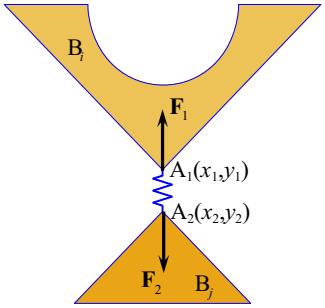

FIGURE 19 Two blocks connected by a spring [Colour figure can be viewed at wileyonlinelibrary.com]

In the same fashion as in Section 5.1 for rock bolt, one can obtain

$$\begin{aligned} k\mathbf{T}_i^{\mathrm{T}}\mathbf{T}_i &\rightarrow \mathbf{K}_{i,i} \\ -k\mathbf{T}_i^{\mathrm{T}}\mathbf{T}_j &\rightarrow \mathbf{K}_{i,j} \\ -k\mathbf{T}_j^{\mathrm{T}}\mathbf{T}_i &\rightarrow \mathbf{K}_{j,i} \\ k\mathbf{T}_j^{\mathrm{T}}\mathbf{T}_j &\rightarrow \mathbf{K}_{j,j} \\ \mathbf{T}_i^{\mathrm{T}}\mathbf{F}_1 &\rightarrow \mathbf{f}_i \\ \mathbf{T}_j^{\mathrm{T}}\mathbf{F}_2 &\rightarrow \mathbf{f}_j, \end{aligned} \tag{86}$$

where k is the stiffness of spring.

5.3 | Beam connector

Now, let us consider 2 particles P_i and P_j bonded together by an elastic beam AB, as shown in Figure 20. Points $\mathrm{A}(x_{\mathrm{A}}, y_{\mathrm{A}})$ and $\mathrm{B}(x_{\mathrm{B}}, y_{\mathrm{B}})$ are the 2 end points of the beam. There is an angle θ between the local coordinate system ξ - η and the global coordinate system x-y. The governing equation of the 2 particles without considering the beam is the same as Equation (73). According to the theory of beam element in FEM, the governing equation in the global coordinate system reads[67]

$$\begin{bmatrix} \mathbf{k}_{1,1}^{\mathrm{Be}} & \mathbf{k}_{1,2}^{\mathrm{Be}} & \mathbf{k}_{1,3}^{\mathrm{Be}} & \mathbf{k}_{1,4}^{\mathrm{Be}} \\ \mathbf{k}_{2,1}^{\mathrm{Be}} & \mathbf{k}_{2,2}^{\mathrm{Be}} & \mathbf{k}_{2,3}^{\mathrm{Be}} & \mathbf{k}_{2,4}^{\mathrm{Be}} \\ \mathbf{k}_{3,1}^{\mathrm{Be}} & \mathbf{k}_{3,2}^{\mathrm{Be}} & \mathbf{k}_{3,3}^{\mathrm{Be}} & \mathbf{k}_{3,4}^{\mathrm{Be}} \\ \mathbf{k}_{4,1}^{\mathrm{Be}} & \mathbf{k}_{4,2}^{\mathrm{Be}} & \mathbf{k}_{4,3}^{\mathrm{Be}} & \mathbf{k}_{4,4}^{\mathrm{Be}} \end{bmatrix} \begin{bmatrix} \mathbf{u}^{\mathrm{A}} \\ \theta^{\mathrm{A}} \\ \mathbf{u}^{\mathrm{B}} \\ \theta^{\mathrm{B}} \end{bmatrix} = \begin{bmatrix} \mathbf{F}^{\mathrm{A}} \\ \mathbf{M}^{\mathrm{A}} \\ \mathbf{F}^{\mathrm{B}} \\ \mathbf{M}^{\mathrm{B}} \end{bmatrix}, \tag{87}$$

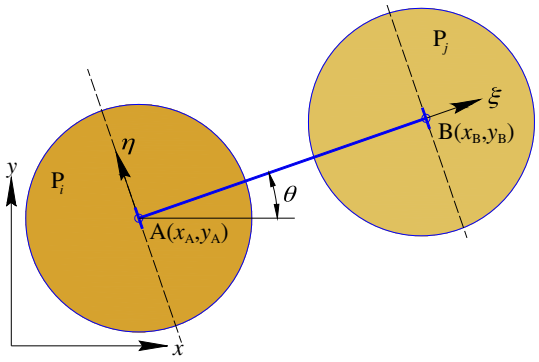

FIGURE 20 Two blocks bonded by a beam [Colour figure can be viewed at wileyonlinelibrary.com]

where $[\mathbf{u}^{\mathrm{A}}, \theta^{\mathrm{A}}, \mathbf{u}^{B}, \theta^{B}]^{\mathrm{T}}$ is the degree of freedom of beam, $[\mathbf{F}^{\mathrm{A}}, \mathbf{M}^{\mathrm{A}}, \mathbf{F}^{B}, \mathbf{M}^{B}]^{\mathrm{T}}$ is equivalent loading vector, and

$$\begin{aligned}
&\mathbf{k}_{1,1}^{\mathrm{Be}} = \begin{bmatrix} A_1\alpha^2 + A_2\beta^2 & (A_1 - A_2)\alpha\beta \\ (A_1 - A_2)\alpha\beta & A_1\beta^2 + A_2\alpha^2 \end{bmatrix}, \quad \mathbf{k}_{1,2}^{\mathrm{Be}} = \begin{bmatrix} A_3\beta \\ -A_3\alpha \end{bmatrix}, \quad \mathbf{k}_{1,3}^{\mathrm{Be}} = \begin{bmatrix} -A_1\alpha^2 - A_2\beta^2 \\ (A_2 - A_1)\alpha\beta \end{bmatrix}, \quad \mathbf{k}_{1,4}^{\mathrm{Be}} = \begin{bmatrix} (A_2 - A_1)\alpha\beta & A_3\beta \\ -A_1\beta^2 - A_2\alpha^2 & -A_3\alpha \end{bmatrix} \\
&\mathbf{k}_{2,1}^{\mathrm{Be}} = \left(\mathbf{k}_{1,2}^{\mathrm{Be}}\right)^{\mathrm{T}}, \quad \mathbf{k}_{2,2}^{\mathrm{Be}} = [A_4], \quad \mathbf{k}_{2,3}^{\mathrm{Be}} = [-A_3\beta], \quad \mathbf{k}_{2,4}^{\mathrm{Be}} = \begin{bmatrix} A_3\alpha & A_5 \end{bmatrix} \\
&\mathbf{k}_{3,1}^{\mathrm{Be}} = \left(\mathbf{k}_{1,3}^{\mathrm{Be}}\right)^{\mathrm{T}}, \quad \mathbf{k}_{3,2}^{\mathrm{Be}} = \left(\mathbf{k}_{2,3}^{\mathrm{Be}}\right)^{\mathrm{T}}, \quad \mathbf{k}_{3,3}^{\mathrm{Be}} = \left[A_1\alpha^2 + A_2\beta^2\right], \quad \mathbf{k}_{3,4}^{\mathrm{Be}} = \begin{bmatrix} (A_1 - A_2)\alpha\beta & -A_3\beta \end{bmatrix} \\
&\mathbf{k}_{4,1}^{\mathrm{Be}} = \left(\mathbf{k}_{1,4}^{\mathrm{Be}}\right)^{\mathrm{T}}, \quad \mathbf{k}_{4,2}^{\mathrm{Be}} = \left(\mathbf{k}_{2,4}^{\mathrm{Be}}\right)^{\mathrm{T}}, \quad \mathbf{k}_{4,3}^{\mathrm{Be}} = \left(\mathbf{k}_{3,4}^{\mathrm{Be}}\right)^{\mathrm{T}}, \quad \mathbf{k}_{4,4}^{\mathrm{Be}} = \begin{bmatrix} A_1\beta^2 + A_2\alpha^2 & A_3\alpha \\ A_3\alpha & A_4 \end{bmatrix},
\end{aligned} \tag{88}$$

$$\begin{aligned}
&A_1 = \frac{EA}{l}, A_2 = \frac{12EI}{(1+b)\,l^3}, \quad A_3 = \frac{6EI}{(1+b)\,l^2}, A_4 = \frac{(4+b)\,EI}{(1+b)\,l}, A_5 = \frac{(2-b)\,EI}{(1+b)\,l} \\
&b = \frac{12k_{\mathrm{Be}}E}{G}\left(\frac{r}{l}\right)^2, \quad \alpha = \cos\theta, \quad \beta = \sin\theta,
\end{aligned} \tag{89}$$

where E, G, A, r, l, and I are Young's modulus, the shear modulus, the area of cross-section, the radius of gyration of cross-section, the length of the beam, and the bending stiffness of section, respectively. For the rectangular cross-section, $k_{\mathrm{Be}} = 1.2$; while for the circular cross-section, $k_{\mathrm{Be}} = 10/9$.

To establish the governing equation considering the beam, we introduce the following matrix:

$$\mathbf{T}_{ij}^{\mathrm{Be}} = \begin{bmatrix} \mathbf{T}_i & 0 \\ \mathbf{E}_i & 0 \\ 0 & \mathbf{E}_j \\ 0 & \mathbf{T}_j \end{bmatrix}. \tag{90}$$

For a rigid particle or block, $\mathbf{E} = [\,0\ 0\ 1\,]$; for a deformable particle, $\mathbf{E} = [\,0\ 0\ 1\ 0\,]$; and for a deformable block, $\mathbf{E} = [\,0\ 0\ 1\ 0\ 0\ 0\,]$. Using the matrix $\mathbf{T}_{ij}^{\mathrm{Be}}$, we can translate the degrees of freedom of the beam into the basic unknown vector of a particle or block, according to

$$\begin{bmatrix} \mathbf{u}^{\mathrm{A}} \\ \theta^{\mathrm{A}} \\ \mathbf{u}^{\mathrm{B}} \\ \theta^{\mathrm{B}} \end{bmatrix} = \begin{bmatrix} \mathbf{T}_i & 0 \\ \mathbf{E}_i & 0 \\ 0 & \mathbf{E}_j \\ 0 & \mathbf{T}_j \end{bmatrix} \begin{bmatrix} \mathbf{d}_i \\ \mathbf{d}_j \end{bmatrix}. \tag{91}$$

The substitution of Equation (91) into Equation (87) and premultiplying by $[\mathbf{T}_{ij}^{\mathrm{Be}}]^{\mathrm{T}}$ gives

$$\begin{aligned}
\mathbf{T}_i^{\mathrm{T}}\mathbf{k}_{1,1}^{\mathrm{Be}}\mathbf{T}_i + \mathbf{E}_i^{\mathrm{T}}\mathbf{k}_{2,1}^{\mathrm{Be}}\mathbf{T}_i + \mathbf{T}_i^{\mathrm{T}}\mathbf{k}_{1,2}^{\mathrm{Be}}\mathbf{E}_i + \mathbf{E}_i^{\mathrm{T}}\mathbf{k}_{2,1}^{\mathrm{Be}}\mathbf{E}_i &\to \mathbf{K}_{i,i} \\
\mathbf{T}_i^{\mathrm{T}}\mathbf{k}_{1,3}^{\mathrm{Be}}\mathbf{T}_j + \mathbf{E}_i^{\mathrm{T}}\mathbf{k}_{2,3}^{\mathrm{Be}}\mathbf{T}_j + \mathbf{T}_i^{\mathrm{T}}\mathbf{k}_{1,4}^{\mathrm{Be}}\mathbf{E}_j + \mathbf{E}_i^{\mathrm{T}}\mathbf{k}_{2,4}^{\mathrm{Be}}\mathbf{E}_j &\to \mathbf{K}_{i,j} \\
\mathbf{T}_j^{\mathrm{T}}\mathbf{k}_{3,1}^{\mathrm{Be}}\mathbf{T}_i + \mathbf{E}_j^{\mathrm{T}}\mathbf{k}_{4,1}^{\mathrm{Be}}\mathbf{T}_i + \mathbf{T}_j^{\mathrm{T}}\mathbf{k}_{3,2}^{\mathrm{Be}}\mathbf{E}_i + \mathbf{E}_j^{\mathrm{T}}\mathbf{k}_{4,2}^{\mathrm{Be}}\mathbf{E}_i &\to \mathbf{K}_{j,i} \\
\mathbf{T}_j^{\mathrm{T}}\mathbf{k}_{3,3}^{\mathrm{Be}}\mathbf{T}_j + \mathbf{E}_j^{\mathrm{T}}\mathbf{k}_{4,3}^{\mathrm{Be}}\mathbf{T}_j + \mathbf{T}_j^{\mathrm{T}}\mathbf{k}_{3,4}^{\mathrm{Be}}\mathbf{E}_j + \mathbf{E}_j^{\mathrm{T}}\mathbf{k}_{4,4}^{\mathrm{Be}}\mathbf{E}_j &\to \mathbf{K}_{j,j} \\
\mathbf{T}_i^{\mathrm{T}}\mathbf{F}^{\mathrm{A}} + \mathbf{E}_i^{\mathrm{T}}\mathbf{M}^{\mathrm{A}} &\to \mathbf{f}_i \\
\mathbf{T}_j^{\mathrm{T}}\mathbf{F}^{\mathrm{B}} + \mathbf{E}_i^{\mathrm{T}}\mathbf{M}^{\mathrm{B}} &\to \mathbf{f}_j.
\end{aligned} \tag{92}$$

6 | COMPOSITE CONTACT MATRIX

6.1 | Node-based composite contact matrix

When a block needs to be subdivided into subelements to enhance the accuracy of strain or stress, this can be done by coupling the FEM with DDA. Consider a block B consisting of a total of l 3-node triangular elements, namely, E_1, E_2, …, E_l, with a total of n nodes. Force $\mathbf{F}$ is the prescribed external loading, and $\mathbf{p}_1$, $\mathbf{p}_2$, …, and $\mathbf{p}_m$ are the unknown contact forces acting on the boundary of the block, as shown in Figure 21.

For an arbitrary point A(x, y) in a 3-node triangular finite element E_k, as shown in Figure 22, the interpolation shape function is given by

$$^{\Delta}\mathbf{T}(x, y) = \left[{}^{\Delta}\mathbf{T}_{n_1}, {}^{\Delta}\mathbf{T}_{n_2}, {}^{\Delta}\mathbf{T}_{n_3}\right], \tag{93}$$

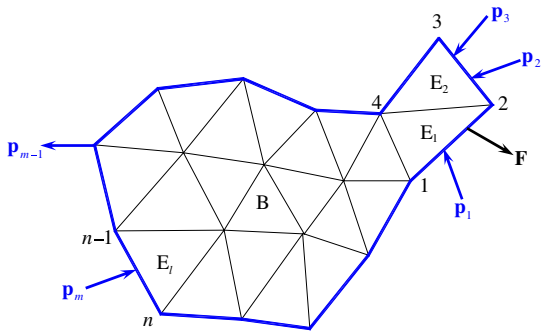

FIGURE 21 A block with subelements [Colour figure can be viewed at wileyonlinelibrary.com]

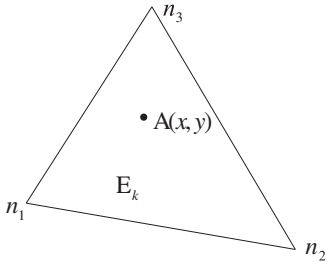

FIGURE 22 A 3-node triangular element

where

$$^{\Delta}\mathbf{T}_i(x, y) = \begin{bmatrix} \phi_i & 0 \\ 0 & \phi_i \end{bmatrix}, \quad i = n_1, n_2, n_3, \tag{94}$$

where $\phi_i (i = n_1, n_2, n_3)$ are the 3 area coordinates of point A(x, y); and n_1, n_2, and n_3 are the global indexes of the nodes with respect to block B (one can refer to the work of Fan et al[68, 69] for more detail). In FEM, the basic unknown is the nodal displacement; the governing equation of motion of the block is expressed as

$$\bar{\mathbf{K}}\bar{\mathbf{d}} - \mathbf{C}^{\text{Node}}\bar{\mathbf{p}} = \bar{\mathbf{f}}, \tag{95}$$

where $\bar{\mathbf{K}}$ is the $2n \times 2n$ equivalent stiffness matrix and $\bar{\mathbf{f}}$ is the $2n$ equivalent nodal loading vector. The equivalent nodal displacement vector $\bar{\mathbf{d}}$ is

$$\bar{\mathbf{d}} = [u_1, v_1, \ \dots \ , u_i, v_i, \ \dots \ , u_n, v_n]^{\mathrm{T}}, \tag{96}$$

where $[u_i, v_i]^{\mathrm{T}}$ is the displacement of ith node and the undetermined contact force vector $\bar{\mathbf{p}}$ reads

$$\bar{\mathbf{p}} = \left[p_1^n, p_1^\tau, \ \dots \ , p_m^n, p_m^\tau\right]^{\mathrm{T}}. \tag{97}$$

In Equation (95), the $2n \times 2$ m matrix $\mathbf{C}^{\text{Node}}$ is called the node-based composite contact matrix, which is closely related to the n nodes of the l elements and the m contact forces.

For any element E_k containing m_1th to m_kth contact pairs (m_1 and m_k are the global indexes of contact forces with respect to the considered block B), we can construct the following triangular element contact matrix:

$$^{\Delta}\mathbf{C} = \left[^{\Delta}\mathbf{C}_{m_1}, \ \dots \ , ^{\Delta}\mathbf{C}_j, \ \dots \ , ^{\Delta}\mathbf{C}_{m_k}\right], \tag{98}$$

where each $^{\Delta}\mathbf{C}_j$ is the 6×2 matrix associated with the jth contact pair on element E_k, and it can be written as

$$^{\Delta}\mathbf{C}_j(x_j, y_j) = s_j \, ^{\Delta}\mathbf{T}_j^{\mathrm{T}}(x_j, y_j)[\mathbf{n}_j, \boldsymbol{\tau}_j], \qquad j = m_1, \ \dots \ , m_k, \tag{99}$$

where (x_j, y_j) is the coordinate of the jth contact point. The sign s_j and matrix $[\mathbf{n}_j, \boldsymbol{\tau}_j]$ are the same as the one in Equation (10).

Substitution of Equation (93) into Equation (99) yields

$$^{\Delta}\mathbf{C}_j(x_j, y_j) = s_j \left[^{\Delta}\mathbf{T}_{n_1}, ^{\Delta}\mathbf{T}_{n_2}, ^{\Delta}\mathbf{T}_{n_3}\right]^{\mathrm{T}}[\mathbf{n}_j, \boldsymbol{\tau}_j], \qquad j = m_1, \ \dots \ , m_k. \tag{100}$$

Thus, we have

$$ {}^{\Delta}\mathbf{C}_{i,j}(x_j, y_j) = s_j {}^{\Delta}\mathbf{T}_i^{\mathrm{T}}(x_j, y_j)[\mathbf{n}_j, \boldsymbol{\tau}_j], \qquad i = n_1, n_2, n_3; \quad j = m_1, \ldots, m_k. \tag{101} $$

Up to now, the node-based composite contact matrix can be defined as

$$ \mathbf{C}^{\mathrm{Node}} = \begin{bmatrix} {}^{\Delta}\mathbf{C}_{1,1} & {}^{\Delta}\mathbf{C}_{1,2} & \cdots & {}^{\Delta}\mathbf{C}_{1,m} \\ {}^{\Delta}\mathbf{C}_{2,1} & {}^{\Delta}\mathbf{C}_{2,2} & \cdots & {}^{\Delta}\mathbf{C}_{2,m} \\ \vdots & \vdots & {}^{\Delta}\mathbf{C}_{i,j} & \vdots \\ {}^{\Delta}\mathbf{C}_{n,1} & {}^{\Delta}\mathbf{C}_{n,2} & \cdots & {}^{\Delta}\mathbf{C}_{n,m} \end{bmatrix}, \qquad i = 1, \ldots, n; \quad j = 1, \ldots, m, \tag{102} $$

where each of the 2×2 submatrix ${}^{\Delta}\mathbf{C}_{i,j} (i = n_1, n_2, n_3; \quad j = m_1, \ldots, m_k)$ is determined by Equation (101). Because $i = n_1$, n_2, n_3, and $j = m_1, \ldots, m_k$ are all the global indexes with respect to block B; therefore, the subscripts i and j are exactly the row index and the column index of ${}^{\Delta}\mathbf{C}_{i,j}$ in $\mathbf{C}^{\mathrm{Node}}$.

To calculate the normal and shear contact gap pertaining to the contact point in a certain element E_k, it is necessary to obtain the nodal displacement vector $\mathbf{d}_k^f$ and the flexibility matrix $\tilde{\mathbf{F}}_k$ for the element E_k. For a noncontact step, from Equation (95), we have

$$ \bar{\mathbf{d}}^f = \bar{\mathbf{K}}^{-1}\bar{\mathbf{f}}. \tag{103} $$

The nodal displacement vector $\mathbf{d}_k^f$ of element E_k can be obtained through

$$ \mathbf{d}_k^f = \begin{bmatrix} \bar{\mathbf{d}}^f[2n_1 - 1 : 2n_1] \\ \bar{\mathbf{d}}^f[2n_2 - 1 : 2n_2] \\ \bar{\mathbf{d}}^f[2n_3 - 1 : 2n_3] \end{bmatrix}, \tag{104} $$

where $\bar{\mathbf{d}}^f[2i - 1 : 2i](i = n_1, n_2, n_3)$ imply the elements of $\bar{\mathbf{d}}^f$ from (2i-1)th to (2i)th. Moreover, n_1, n_2, and n_3 are the global indexes of the nodes. While the flexibility matrix $\tilde{\mathbf{F}}_k$ of element E_k is given by

$$ \tilde{\mathbf{F}}_k = \begin{bmatrix} \bar{\mathbf{K}}^{-1}[2n_1 - 1 : 2n_1, :] \\ \bar{\mathbf{K}}^{-1}[2n_2 - 1 : 2n_2, :] \\ \bar{\mathbf{K}}^{-1}[2n_3 - 1 : 2n_3, :] \end{bmatrix} \mathbf{C}^{\mathrm{Node}}, \tag{105} $$

where $\bar{\mathbf{K}}^{-1}[2i - 1 : 2i, :](i = n_1, n_2, n_3)$ denote all column elements from (2i-1)th to (2i)th row of $\bar{\mathbf{K}}^{-1}$ and n_1, n_2, and n_3 are also the global indexes of the nodes. Here, note that the "double contact displacement" should be adopted as well to avoid the "one-step lag."

6.2 | Particle/block-based composite contact matrix

Some particles or blocks can be connected by bolts, springs, or beams to build up an assembly, as shown in Figure 23. Assume that the total number of particles and blocks is n, namely, $\mathrm{B}_1, \mathrm{B}_2, \ldots, \mathrm{B}_n$, the force $\mathbf{F}$ is the prescribed external loading, and $\mathbf{p}_1, \mathbf{p}_2, \ldots$, and $\mathbf{p}_m$ are the unknown contact forces acting on the assembly. The governing equation is

$$ \breve{K}\breve{\mathbf{d}} - \mathbf{C}^{\mathrm{P/b}}\breve{\mathbf{p}} = \breve{\mathbf{f}}, \tag{106} $$

where $\breve{\mathbf{K}}$ is the equivalent stiffness matrix and $\breve{\mathbf{f}}$ is the equivalent loading vector. The equivalent basic known vector $\breve{\mathbf{d}}$ is

$$ \breve{\mathbf{d}} = [\mathbf{d}_1, \ldots, \mathbf{d}_i, \ldots, \mathbf{d}_n]^{\mathrm{T}}, \tag{107} $$

where $\mathbf{d}_i$ corresponds to the ith particle or block B_i. The undetermined contact force vector $\breve{\mathbf{p}}$ is

$$ \breve{\mathbf{p}} = \left[p_1^n, p_1^\tau, \ldots, p_m^n, p_m^\tau\right]^{\mathrm{T}}. \tag{108} $$

In Equation (106), the matrix $\mathbf{C}^{\mathrm{P/b}}$ is called the particle/block-based composite contact matrix, which is given by

$$ \mathbf{C}^{\mathrm{P/b}} = \begin{bmatrix} \mathbf{C}_1 & & & \\ & \ddots & & \\ & & \mathbf{C}_i & \\ & & & \ddots \\ & & & & \mathbf{C}_n \end{bmatrix}, \qquad i = 1, \ldots, n, \tag{109} $$

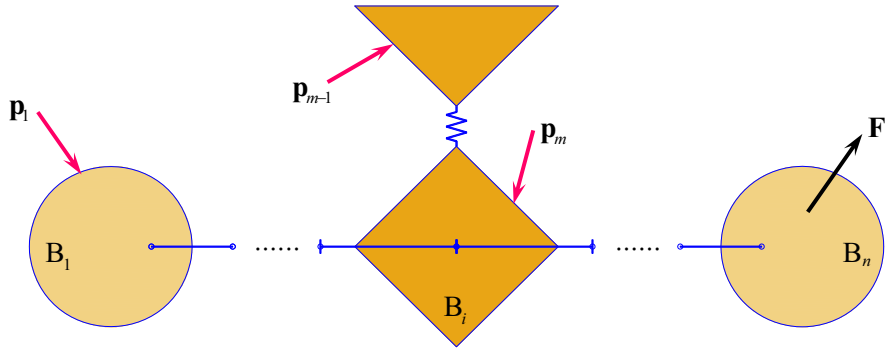

FIGURE 23 An assembly of particles and blocks [Colour figure can be viewed at wileyonlinelibrary.com]

where $\mathbf{C}_i$ is the contact matrix for the particle or block and is determined by Equation (9).

To estimate the normal or shear contact gap for a contact point pertaining to a certain particle or block B_i, we have to solve the known vector $\tilde{\mathbf{d}}_i^f$ and the flexibility matrix $\tilde{\mathbf{F}}_i$ for block B_i. For the noncontact step, from Equation (106), we have

$$\breve{\mathbf{d}}^f = \breve{\mathbf{K}}^{-1}\breve{\mathbf{f}}, \tag{110}$$

and

$$\mathbf{d}_i^f = \left[\breve{\mathbf{d}}^f\left[k_0(i-1)+1 : k_0 i\right]\right], \tag{111}$$

where $\breve{\mathbf{d}}^f[k_0(i-1)+1 : k_0 i](i = 1, \ldots, n)$ stand for the elements of $\breve{\mathbf{d}}^f$ from $k_0(i\text{-}1) + 1$th to $k_0 i$th. For an assembly consisting of rigid particles and blocks only, $k_0 = 3$; for one with deformable particles, $k_0 = 4$; and $k_0 = 6$ for an assembly comprised of deformable blocks. The flexibility matrix $\tilde{\mathbf{F}}_i$ of block B_i is

$$\tilde{\mathbf{F}}_i = \left[\breve{\mathbf{K}}^{-1}[k_0(i-1)+1 : k_0 i, :]\right]\mathbf{C}^{\mathrm{P/b}}, \qquad i = 1, \ldots, n, \tag{112}$$

where $\breve{\mathbf{K}}^{-1}[k(i-1)+1 : ki, :](i = 1, \ldots, n)$ signify all column elements from $k_0(i\text{-}1) + 1$th to $k_0 i$th row of $\breve{\mathbf{K}}^{-1}$. Then, the compatibility iteration is employed to solve the unknown contact forces.

If there are m rolling resistances, the following particle/block-based composite rolling resistance matrix $\mathbf{R}^{\mathrm{P/b}}$ should be used:

$$\mathbf{R}^{\mathrm{P/b}} = \begin{bmatrix} \mathbf{R}_1 & & & \\ & \ddots & & \\ & & \mathbf{R}_i & \\ & & & \ddots \\ & & & & \mathbf{R}_m \end{bmatrix}, \qquad i = 1, \ldots, m, \tag{113}$$

where $\mathbf{R}_i(i = 1, \ldots, m)$ is determined by Equation (50). To form the corresponding equivalent rolling resistance vector, Equations (47), (49), and (59) can be used.

7 | NUMERICAL EXAMPLES

In this section, several interesting and challenging examples are designed to validate the potential of the new DDA. For convenience, DDA_0 denotes the original DDA[31] for an arbitrary shape block with first-order displacement field. D-DDA refers to the DDA[53] with rigid disks only. DDA-d stands for the modified DDA described in the work of Zheng et al,[56] while PB-DDA stands for the proposed DDA in this study. In the following examples, an extremely large density is adopted for a static particle or block to avoid the introduction of additional energy caused by the usage of fixed springs.

7.1 | Static heap of 3 disks

The first problem to be considered is a static heap formed by 3 disks, as shown in Figure 24. Three rigid disks of the same size are placed over one another vertically on a fixed horizontal base before the gravity is switched on. The weights of the 3 disks are $\mathbf{G}_1$, $\mathbf{G}_2$, and $\mathbf{G}_3$, respectively. An idealized configuration is employed to test the proposed algorithm. Let the radius of all 3 disks $R = 10.0$ m and their material density is the same $\rho = 2500$ kg/m^3. Assume the acceleration of

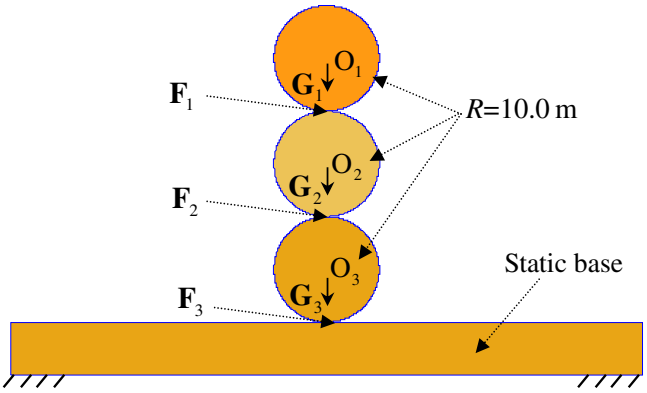

FIGURE 24 Configuration of 3-disk heaping [Colour figure can be viewed at wileyonlinelibrary.com]

TABLE 1 Contact forces $\mathbf{F}_1$, $\mathbf{F}_2$, and $\mathbf{F}_3$ corresponding to CS = 100 (see Figure 24)

Contact force, N	Penalty value (Pa) used by D-DDA 0.10×10^{12}	0.10×10^{13}	0.10×10^{14}	0.10×10^{15}	PB-DDA
$\boldsymbol{F}_1$	7 853 981.63397	7 853 981.61908	7 853 981.62785	7 853 981.01220	7 853 981.63323
AE	−110.18062	−0.01489	−0.00613	−0.62177	−0.00075
$\boldsymbol{F}_2$	15 707 963.26795	15 707 963.22662	15 707 963.27239	15 707 969.45410	15 707 963.26647
AE	−380.73067	−0.04133	0.00444	6.18615	−0.00148
$\boldsymbol{F}_3$	23 561 944.90192	23 561 944.77060	23 561 944.81216	23 561 950.83944	23 561 944.89971
AE	−467.90848	−0.13132	−0.08976	5.93752	−0.00222

Note: Analytical solution (N): $\mathbf{F}_1 = 7\,853\,981.63397$; $\mathbf{F}_2 = 15\,707\,963.26795$; $\mathbf{F}_3 = 23561944.90192$. Abbreviations: AE, absolute error; CS, calculation step; D-DDA, discontinuous deformation analysis with rigid disks; DDA, discontinuous deformation analysis; PB-DDA, particle-block discontinuous deformation analysis.

gravity $g = -10$ m/s^2. An extremely large density $\rho_b = 10^{11}\rho$ is assumed for the base to render it stationary. A time step length $\boldsymbol{\Delta} = 0.001$ s is adopted. A zero-order displacement approximation is adopted in the PB-DDA. In the following simulations, several penalty parameters $P = 0.10\times10^{12}$, 0.10×10^{13}, 0.10×10^{14}, and 0.10×10^{15} Pa are used by the D-DDA to observe the stability of the 3 disks. If the system is stable, it is evident that contact forces $\mathbf{F}_1 = \mathbf{G}_1$, $\mathbf{F}_2 = \mathbf{G}_1 + \mathbf{G}_2$, and $\mathbf{F}_3 = \mathbf{G}_1 + \mathbf{G}_2 + \mathbf{G}_3$, respectively. Some representative values for contact forces obtained from the D-DDA and PB-DDA are listed in Table 1. Evidently, the absolute errors of contact forces obtained by D-DDA do not show a consistent negative correlation with the penalty value since, when the penalty number is increased to $P = 0.10\times10^{15}$ Pa, the absolute errors blow up again. However, since no contact penalty is needed in PB-DDA, the absolute accuracy is improved almost one order of magnitude compared with the best case by D-DDA ($P = 0.10\times10^{14}$ Pa).

7.2 | Static stability of 4 blocks

A second example to be considered is the static stability of 4 identical blocks B_1, B_2, B_3, and B_4 stacked, as shown in Figure 25, on a static horizontal base. The length and width of the blocks are 20.0 m, and 10.0 m, respectively. The staggering distance is 5.0 m. The gravity is the only external force loaded on them. The forces $\mathbf{F}_1$ and $\mathbf{F}_2$ are the contact forces acting on block B_4 at points A_1 and A_2, respectively. Under the given geometric conditions and statics relation with positive contact forces $\mathbf{F}_1$ and $\mathbf{F}_2$, the 4 blocks are theoretically stable. The material density of the blocks is $\rho = 2000$ kg/m^3. The acceleration of gravity is set $g = -10$ m/s^2, and the time step $\boldsymbol{\Delta} = 0.001$ second. To avoid the motion of base, a big material density is given for the base at $\rho_b = 10^{11}\rho$, and its weight is ignored. The computations of DDA_0, and PB-DDA adopt Young's modulus $E = 0.10\times10^{15}$ Pa and Poisson's ratio $\upsilon = 0.45$. In this example, 4 cases of penalty parameters $P = 0.10\times10^{12}$, 0.10×10^{13}, 0.20×10^{14}, and 0.10×10^{15} Pa are considered in the DDA_0. Table 2 summarizes typical contact forces $\mathbf{F}_1$ and $\mathbf{F}_2$ obtained by the 2 approaches. When $P = 0.10\times10^{12}$ Pa, the calculations by DDA_0 suggest that the 4 blocks are stable, but the obtained contact forces indicate otherwise. When $P \geq 0.10\times10^{13}$ Pa, the values of the contact forces obtained by DDA_0 are consistent with its analysis result. There is no apparent correlation between the penalty

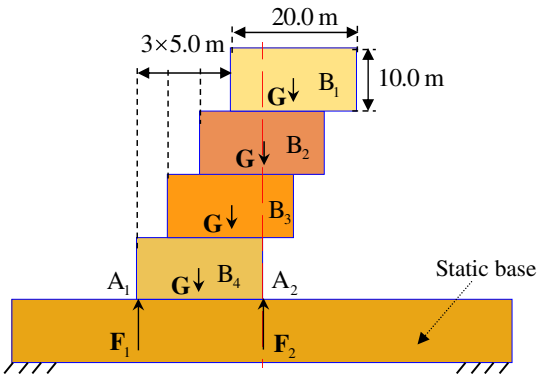

FIGURE 25 Configuration of 4 blocks [Colour figure can be viewed at wileyonlinelibrary.com]

TABLE 2 Contact forces $\mathbf{F}_1$ and $\mathbf{F}_2$ corresponding to CS = 100 (see Figure 25)

Contact force, N	Penalty value (Pa) used by DDA_0				PB-DDA
	0.10×10^{12}	0.10×10^{13}	0.20×10^{14}	0.10×10^{15}	
$\mathbf{F}_1$	7556.48247	999 999.99724	1 000 000.61471	1 000 000.06365	1 000 000.02319
AE	−992 443.51753	−0.00276	0.61471	0.06365	0.02319
$\mathbf{F}_2$	7603.17995	999 999.99724	6 999 996.57054	6 999 999.84910	6 999 999.88567
AE	−6 992 396.82005	−6 000 000.00276	−3.42946	−0.15090	−0.11433

Note: Analytical solution (N): $\mathbf{F}_1 = 1\,000\,000.00000$; $\mathbf{F}_2 = 7\,000\,000.00000$. Abbreviations: AE, absolute error; CS, calculation step; DDA, discontinuous deformation analysis; PB-DDA, particle-block discontinuous deformation analysis.

parameter and the contact forces obtained by DDA_0. On the other hand, the PB-DDA can help obtain the contact forces with relatively better precision.

7.3 | Reciprocal motion of a ring particle within a frame

In this example, we consider the undulation motion of a ring particle in a frame to examine the "one-step lag" phenomenon and the effectiveness of its treatment by the "double contact displacement" approach. Suppose the inner and external diameters of the ring particle are 2.0 m and 6.0 m, respectively. At initial time, the ring particle is located at the centroid of a quadrate frame (the inner side length is equal to 40.0 m), which is kept static. Moreover, the initial velocity of the ring particle is set as $\mathbf{v} = (2.5, 5.0)$ m/s. Both the particle and the frame are assumed to be rigid bodies. Neither external force nor friction is considered. Due to the conservation of momentum, the ring particle will undergo reciprocal motion along the blue dash line, as shown in Figure 26, along which there are 6 inflection points marked by "*." The time step is chosen as $\mathbf{\Delta} = 0.05$ second, and the total calculation step is CS = 2050. The predictions are shown in Figure 27.

In designing the example in Figure 26, we specifically assume that both components of the initial velocity are nonzero and demonstrate the "one-step lag" prediction by DDA-d.[56] This makes the displacement in the normal direction remain

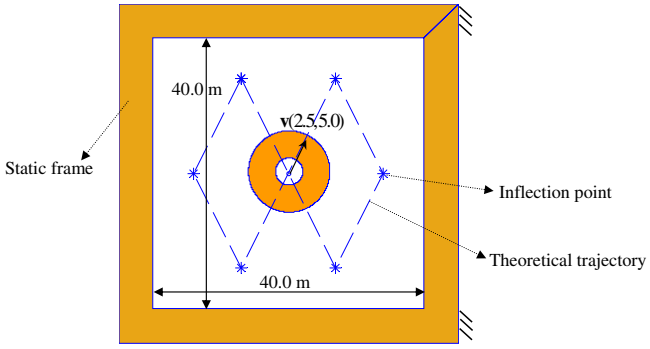

FIGURE 26 Configuration of a circle particle in a quadrate frame

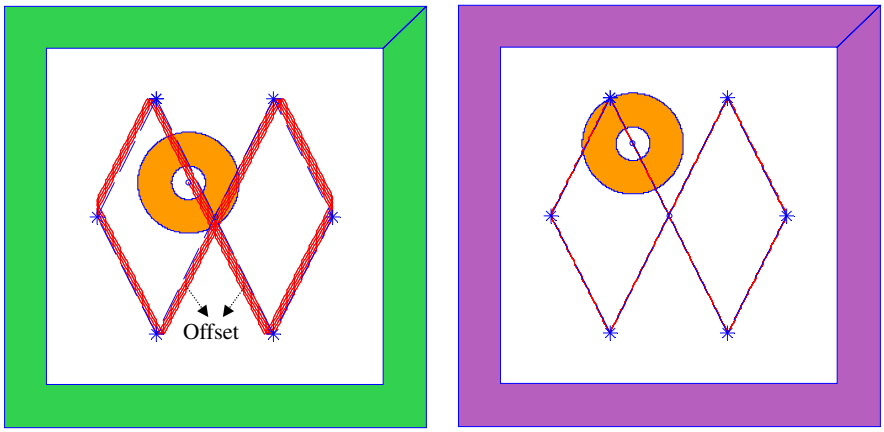

FIGURE 27 Reciprocating motion of a particle. A, Prediction by DDA-d; B, Prediction by PB-DDA

always one time step behind the displacement in the shear direction. The trajectory (the red solid line in Figure 27A) of the particle predicted by the DDA-d shows apparent deviations from the theoretical trajectory (the blue dash line in Figure 27A). On the other hand, the PB-DDA improved by the "double contact displacement" technique can provide nearly identical predictions with the theoretical solution, as shown in Figure 27B.

7.4 | Cyclic motion of a block

A third case treated here is the cyclic motion of a block within a static quadrate framework, as shown in Figure 28, to validate the conservation of momentum. The internal side length of the quadrate framework is 120.0 m, while the side length of the block is 20.0 m. At the initial time, the centroid of the block coincides with that of the framework, ie, point O. The initial velocity of the block is given by $\mathbf{v} = (2.5, 5.0)$ m/s (denoting horizontal and vertical components of the velocity, respectively). No external local is considered in this example. Due to the conservation of momentum, the block will undergo periodical translational motion along the blue dash line, along which there are 6 inflection points marked by "*." For both the block and the framework, Young's modulus $E = 0.50 \times 10^{14}$ Pa and Poisson's ratio $\upsilon = 0.35$ are adopted. The material density of block is set to $\rho = 2300$ kg/m^3 and that of the framework to $\rho_f = 10^9 \rho$. The framework is assumed to be motionless. The time step is $\mathbf{\Delta} = 0.01$ second. Five sets of penalty parameters are adopted by the DDA$_0$, ie, $P = 0.10 \times 10^{12}$, 0.10×10^{13}, 0.10×10^{14}, 0.10×10^{15}, and 0.10×10^{16} Pa. The trajectory of point O is shown in Figure 29.

Notably, the predictions by DDA$_0$ and PB-DDA are different. When $P = 0.10 \times 10^{12}$, only the first segment AB of the trajectory (the red solid line) for point O predicted by DDA$_0$ is correct (see Figure 29A). While for the other 4 cases of penalty parameters, only the initial segments ABCD of the trajectory of point O predicted by DDA$_0$ coincide with the theoretical trajectory (the blue dash line), and apparent block rotation is found in all 4 cases (see Figure 29B, 29C, 29D, and 29E). In contrast, the predicted trajectory of point O by PB-DDA agrees well with the theoretical trajectory, and the

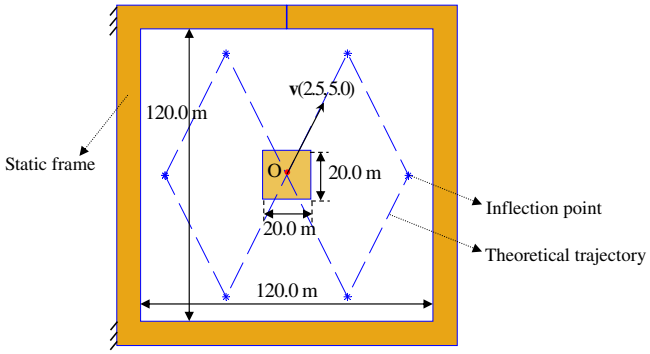

FIGURE 28 Configuration of a block in a quadrate framework

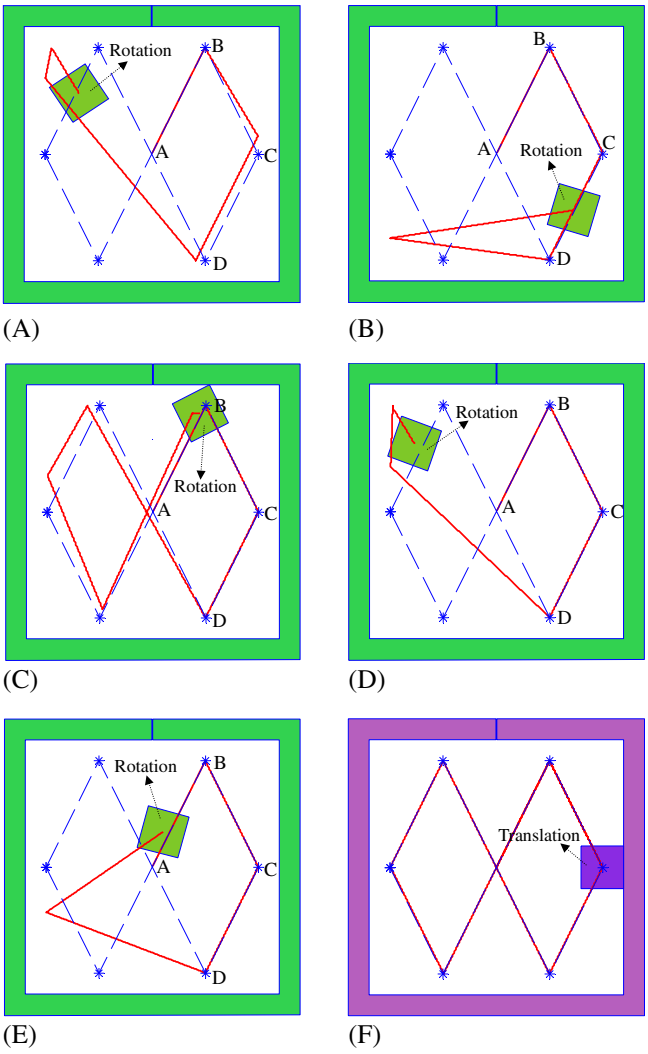

FIGURE 29 Trajectories of point O predicted by DDA_0 in A, B, C, D, and E and by PB-DDA in F. A, $P = 0.1 \times 10^{12}$ Pa, CS = 10 000; B, $P = 0.1 \times 10^{13}$ Pa, CS = 10 000; C, $P = 0.1 \times 10^{14}$ Pa, CS = 10 000; D, $P = 0.1 \times 10^{15}$ Pa, CS = 10 000; E, $P = 0.1 \times 10^{16}$ Pa, CS = 10 000; F, P is not needed, CS = 10 000

block undergoes translational motion only, as shown in Figure 29F. Indeed, since DDA_0 does not refer to the acceptable contact force, the conversation of momentum is satisfied only at the initial stages corresponding to segments ABCD of the trajectory. Therefore, the trajectory of the block may not be faithfully predicted, especially for later stage of the simulation. In particular, it is also difficult to determine an appropriate penalty parameter for DDA_0 in such cases. The PB-DDA clearly helps us avoid this issue.

7.5 | Rolling of a disk on a frictionless surface inside a ring

Figure 30 presents a disk O_1 is initially located inside a ring O_2 at point A (−60.0, 0.0) where points A, O_1, and O_2 are on the same horizontal line AO_1O_2. The radii of the disk and the inner ring are given by $R_1 = 40.0$ m and $R_2 = 100.0$ m, respectively. The material density of the disk $\rho = 1$ kg/m^3, and the material density of ring adopts an extreme value of $\rho_r = 10^{12}\rho$ to prevent the motion of ring. Gravity and friction are not considered for the ring. The acceleration of gravity $g = -10$ m/s^2. Both the disk and the ring are assumed to be rigid. The time step is set to $\mathbf{\Delta} = 0.005$ second, and the total calculation step CS = 4 000. Under gravity, the disk will move periodically along the bottom half circle of the ring, with a theoretical curve of contact force depicted in Figure 31. During the first semiperiod at the time $t_1 = 4.675$ seconds, the maximum contact force predicted by PB-DDA is $\mathbf{F}_{max1} = 150\,803.493116$ N, which agrees well with the theoretical solution $\mathbf{F} = 3\,mg = 150\,796.447372$ N. During the second semiperiod at the time $t_2 = 14.025$ seconds, the maximum contact force is $\mathbf{F}_{max2} = 150\,796.553208$ N, which is almost identical with the theoretical solution $\mathbf{F} = 3\,mg = 150\,796.447372$ N. The

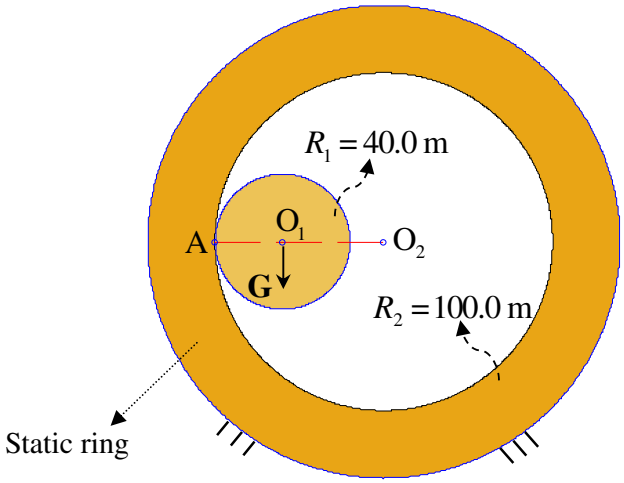

FIGURE 30 Configuration of a disk in a ring [Colour figure can be viewed at wileyonlinelibrary.com]

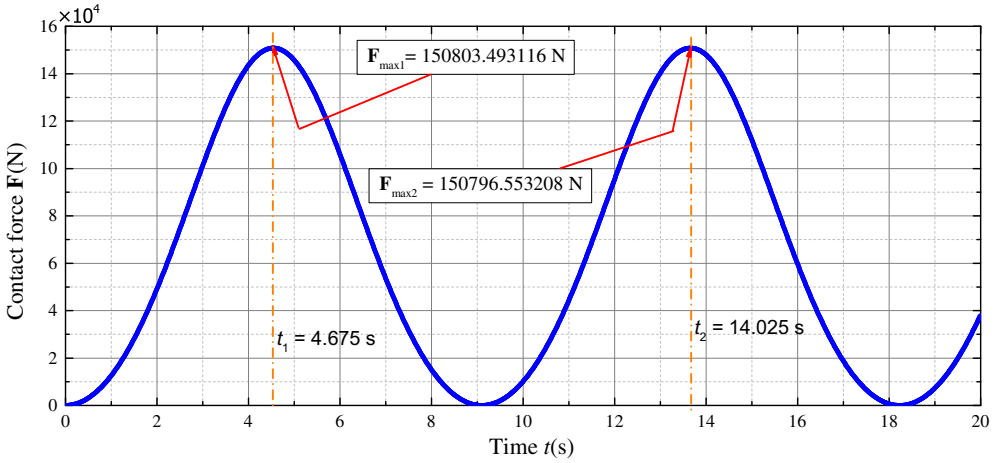

FIGURE 31 Contact force versus time [Colour figure can be viewed at wileyonlinelibrary.com]

predicted trajectory of point O_1 by PB-DDA is shown in Figure 32. It is observed that the disk may climb up to the same height at point O_1* on the right-hand side as its releasing point O_1, and then go back to point O_1 again, which implies both the mechanical energy and the moment of the system are conservative by the proposed algorithm.

7.6 | Sliding motion of a block on frictional surface

A further example of block with a side length of $l = 1.0$ m sliding on friction surface of a static block is investigated, as shown in Figure 33. Contacts V_1-BC_{-BB} and V_2-BC_{-BB} are the pairs of adjoint vertex-edge contacts. **G** is the gravity. A given tractive force $\mathbf{F} = 1000$ N is applied to point A. The contact forces $\mathbf{F}_{n1}$, $\mathbf{F}_{s1}$, $\mathbf{F}_{n2}$, and $\mathbf{F}_{s2}$ are undetermined. Both blocks are assumed to be rigid body. For the smaller block, the material density is specified at $\rho = 1000$ kg/m^3, and the acceleration of gravity $g = -10$ m/s^2. For the bigger block, the material density of block is given by $\rho_b = 10^{12}\rho$. The time step is set to be $\mathbf{\Delta} = 0.01$ second. In order to exam the relative motions between the 2 contact pairs, we set the eccentric distance $d = 0.7$ m, the sliding friction coefficient $\mu = 0.0$, and the cohesion $c = 400$ N. The predicted results are shown in Table 3. In DDA-d, because the shear ratio between the adjoint vertex-edge contacts is ignored, the over-resistance to the sliding arises, which leads to incorrect predictions of the normal and shear contact forces by DDA-d. In contrast, the contact forces predicted by the PB-DDA agree rather well with the theoretical solutions.

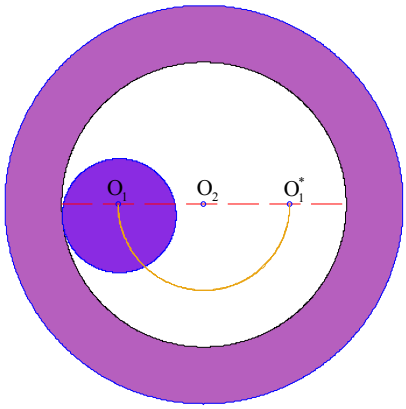

FIGURE 32 Trajectory of point O_1 predicted by particle-block discontinuous deformation analysis [Colour figure can be viewed at wileyonlinelibrary.com]

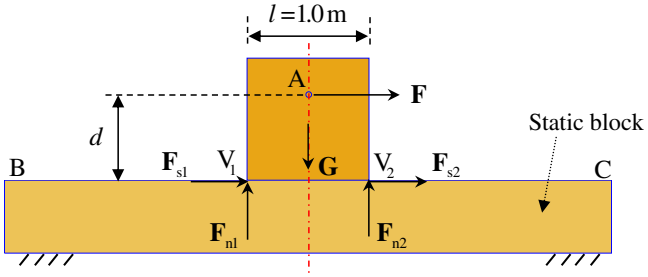

FIGURE 33 Configuration of a block on friction surface [Colour figure can be viewed at wileyonlinelibrary.com]

TABLE 3 Contact forces for cohesion $c = 400$ N (see Figure 33)

	Contact force F_{n1}, N		Contact force F_{n2}, N		Contact force $F_{s1} + F_{s2}$, N	
	DDA-d	PB-DDA	DDA-d	PB-DDA	DDA-d	PB-DDA
CV	4400.00001	4599.99999	5599.99999	5399.99999	−800.00000	−400.00000
TS	4600.00000	4600.00000	5400.00000	5400.00000	−400.00000	−400.00000
AE	−199.99999	−0.00001	199.99999	−0.00001	−400.00000	0.00000

Abbreviations: AE, absolute error; CV, calculation value; DDA-d, dual formation of discontinuous deformation analysis; PB-DDA, particle-block discontinuous deformation analysis; TS, theoretical solution.

7.7 | Rolling motion of a disk on frictional surface

In this example, we consider the rolling motion of a disk of $R = 1.0$ m over the frictional surface of a static block, as shown in Figure 34. Points A and O are taken as 2 monitoring points. The material density of the disk is set to be $\rho = 1000$ kg/m^3 and the acceleration of gravity $g = -10$ m/s^2. In PB-DDA, the disk is treated as a rigid body, while the block is assumed deformable, and its gravity is not considered. The material density of block is given by $\rho_b = 10^{12}\rho$; its Young's modulus is set to $E = 0.10 \times 10^{10}$ Pa and its Poisson's ratio $\upsilon = 0.25$. The time step is set to be $\mathbf{\Delta} = 0.01$ second. Under the gravity $\mathbf{G}$, a given tractive force $\mathbf{F} = 1000$ N, and the unknown contact force, the disk will move rightwards. Several cases of distance $d = 0.0$, 0.5, 1.0, 1.5, and 2.0 m between the line of action of the force $\mathbf{F}$ are explored. The contact surface AB is adopted to test the pure rolling motion of the disk. The major results are summarized in Table 4. The predicted maximum normal contact force $\mathbf{F}_n$ by the PB-DDA has an absolute error of 0.00182 N as compared with the theoretical value, while that for the shear contact force is 0.00001 N, showing rather accurate predictions by the PB-DDA.

Meanwhile, to examine the rolling resistance effect, a large rolling friction coefficient $\delta = 1.0$ m is adopted (which means that the rang of value of rolling resistance moment is limited between -1$\mathbf{G}$ and 1$\mathbf{G}$ while the disk remains static). The predicted results are summarized in Table 5. At difference distance d, PB-DDA realistically predicts appropriate rolling resistance moment in resisting the rolling motion of the disk. The displacements of points A and O, namely, $\mathbf{U}_A$ and $\mathbf{U}_O$, are predicted to be zero, implying no move for the 2 points as expected.

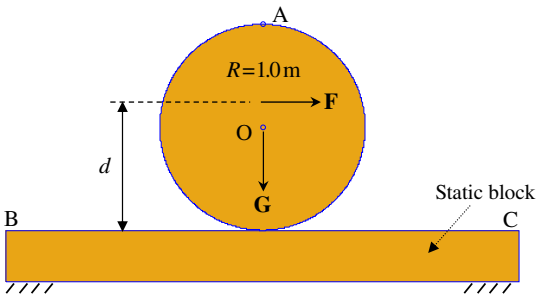

FIGURE 34 Configuration of a disk rolling along a frictional surface [Colour figure can be viewed at wileyonlinelibrary.com]

TABLE 4 Contact force for the pure rolling motion of a disk (see Figure 34)

Contact force, N	Distance *d*, m 0.0	0.5	1.0	1.5	2.0
$\mathbf{F}_n$	31 415.92836	31 415.92714	31 415.92654	31 415.92654	31 415.93015
TS			**G**		
AE	0.00182	0.00060	0.00000	0.00000	0.00361
$\mathbf{F}_s$	−1000.00001	−666.66666	−333.33334	0.00000	333.33333
TS	-**F**	-2**F** /3	-**F** /3	0	**F** /3
AE	−0.00001	0.00001	−0.00001	0.00000	−0.00001

Note: **G** = 31 415.92654 N; **F** = 1000.0 N; $\mathbf{F}_n$, normal contact force; $\mathbf{F}_s$, shear contact force. Abbreviations: AE, absolute error; TS, theoretical solution.

TABLE 5 Rolling resistance to a disk (see Figure 34)

Rolling resistance	Distance *d*, m 0.0	0.5	1.0	1.5	2.0
θ_0(rad)	0.0	−0.000005	−0.000011	−0.000016	−0.000021
$\mathbf{M}_r$(N·m)	0.0	499.99975	999.99959	1499.99938	1999.99914
$\mathbf{F}_r$(N)	0.0	−0.33333	−0.66667	−1.00000	−1.33333
$\mathbf{U}_A$(m)	0.0	0.0	0.0	0.0	0.0
$\mathbf{U}_O$(m)	0.0	0.0	0.0	0.0	0.0

Note: θ_0, initial rolling angle; $\mathbf{M}_r$, rolling resistance moment; $\mathbf{F}_r$, rolling resistance force; $\mathbf{U}_A$, displacement of point A; $\mathbf{U}_O$, displacement of point O.

To investigate the motion of the disk, we further fix d = 1.0 m, and the total calculation step CS = 500, and consider the following 3 cases. (I) The sliding friction coefficient is specified at a large value at μ= 10.0 and the rolling friction coefficient δ= 0.0 m, which renders the disk to undergo pure rolling. (II) The sliding friction coefficient is set at μ= 0.005 and the rolling friction coefficient at δ= 0.005 m. The disk will undergo both sliding and rolling in this case. (III) The sliding friction coefficient is set at μ= 0.005 and the rolling friction coefficient at δ= 0.0 m, whereby no rolling resistance is considered. The trajectories of points A and O are shown in Figure 35.

When CS = 500, points A and O reach points A* and O*, respectively (see Figure 35). For the pure rolling, namely, case I, the length of the blue trajectory OO* is the shortest, while the curvature of the blue trajectory AA* is the biggest. As can be seen, due to the decrease in sliding friction coefficient and increased rolling resistance, the red trajectory OO* in case III is the longest and the curvature of the red trajectory AA* is the smallest. For case II, the length of the green straight OO* and the curvature of the green curve AA* are in between cases I and III.

7.8 | Two blocks connected by a cemented interface

Figure 36 shows 2 blocks B_1 and B_2 connected by a cemented interface C_1C_2, which is designed to validate the cemented interface model of our new PB-DDA. Lines AB and CD are the geometric symmetry lines of block B_2. The half-height of block B_2 is H = 1.0 m. As we proposed, the cemented interface C_1C_2 is made equivalent by 2 joints C_1 and C_2. The action point of force **F** is on line CD and in parallel with line AB, with a vertical distance between the line of action of

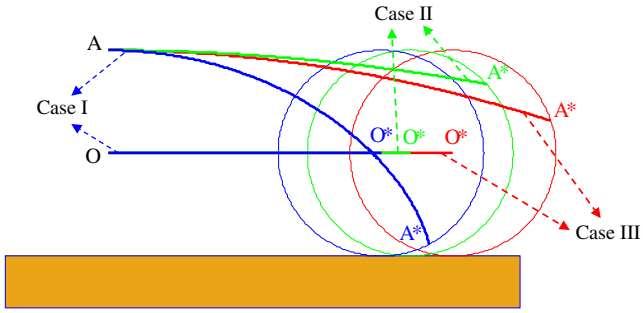

FIGURE 35 Trajectories of points A and O corresponding to 3 cases obtained by particle-block discontinuous deformation analysis

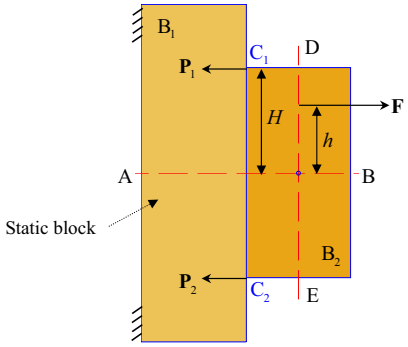

FIGURE 36 Configuration of blocks connected by the cementing interface [Colour figure can be viewed at wileyonlinelibrary.com]

TABLE 6 Interface tensions (see Figure 36)

Interface tension, N	t = 2,000 N		
	h = 0.0 m	h = 0.5 m	h = 1.0 m
$\mathbf{P}_1$	−499.99999	−750.00001	−999.99999
TS	−500.00000	−750.00000	−1000.00000
AE	0.00001	−0.00001	0.00001
$\mathbf{P}_2$	−499.99999	−249.99999	−0.00001
TS	−500.00000	−250.00000	0.00000
AE	0.00001	0.00001	−0.00001

Abbreviations: AE, absolute error; TS, theoretical solution.

F and line AB by h. In our simulation, it is assumed that **F** = 1000 N, the material density of block B_2 ρ = 1000 kg/m^3, and the gravity is ignored. Block B_1 is assumed to be fixed without motion. In addition, the 2 blocks are considered as nondeformable. The time step is set to 0.01 second; the tensile strength of cementing material is given by t = 2000 N. The interface tensile forces $\mathbf{P}_1$ and $\mathbf{P}_2$ are predicted when B_2 is subjected to **F**, and the results are summarized in Table 6. Evidently, the numerical predictions by PB-DDA are rather close to the theoretical solutions.

7.9 | Undulation motion of a circle particle

The bouncing motion of a particle between 2 static blocks, as shown in Figure 37, is taken as an example to examine the node-based composite contact matrix. A particle of radius r = 0.5 m is assumed to be initially located in between 2 blocks ($H_1 = H_2$ = 0.5 m). Both blocks are supposed to be static, and the bottom block is subdivided into subelements. Both the upper block and the particle are treated as rigid bodies, while the bottom block with a Young's modulus $E = 0.10 \times 10^{15}$ Pa and a Poisson's ratio υ= 0.45. Therefore, its deformation can be ignored; this is appropriate for examining the node-based composite contact matrix. The material density of the particle ρ = 2500 kg/m^3, and its gravity is ignored. The initial velocity of the particle is set to be $\mathbf{V}_0 = (v_{0x}, v_{0y}) = (v_{0x} = 1.0, v_{0y} = 1.0, 2.0, \text{or } 3.0)$ m/s. The time step is set to be 0.05 second, and the total time is equal to 1.0 second. Therefore, the particle will arrive to point B (the distance between points A

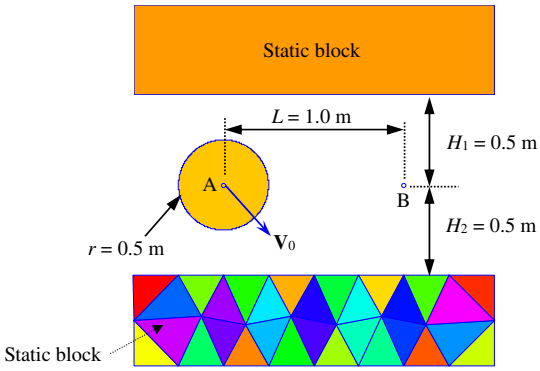

FIGURE 37 Configuration of the reciprocating motion of a particle [Colour figure can be viewed at wileyonlinelibrary.com]

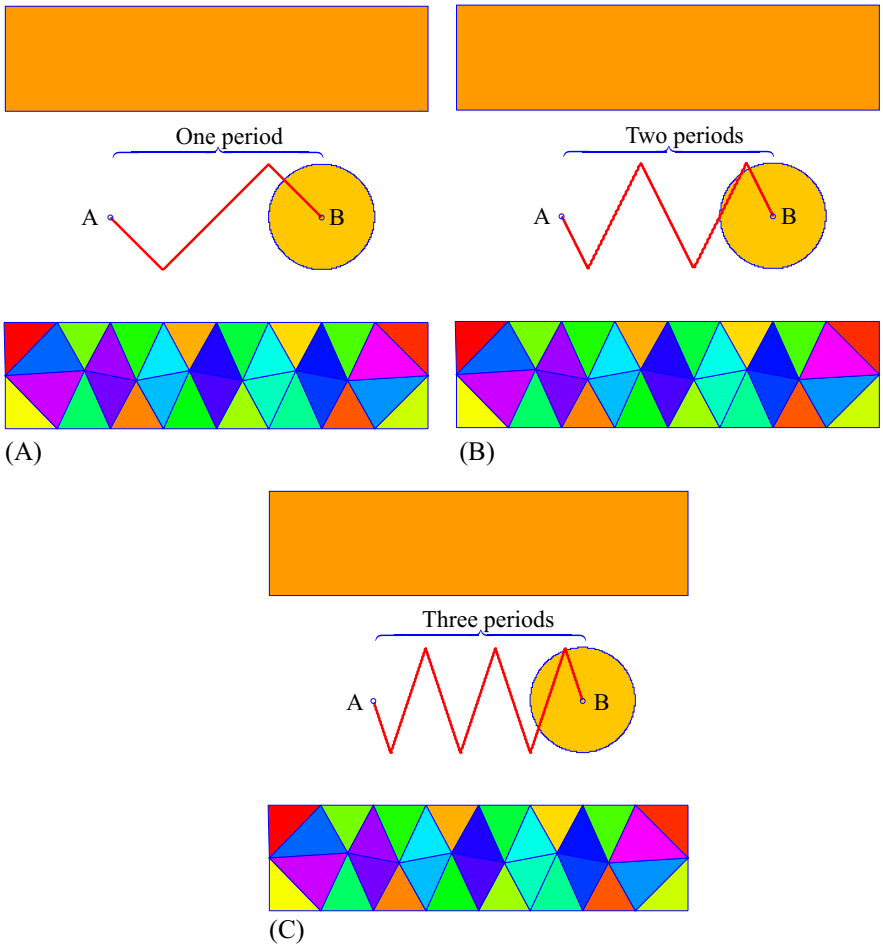

FIGURE 38 Undulation motion of a particle between 2 blocks. A, $\mathbf{V}_0 = (1.0, 1.0)$ m/s; B, $\mathbf{V}_0 = (1.0, 2.0)$ m/s; C, $\mathbf{V}_0 = (1.0, 3.0)$ m/s [Colour figure can be viewed at wileyonlinelibrary.com]

and B is $L = 1.0$ m) after several collisions, the times of which depends on the value v_{0y}. When $\mathbf{V}_0 = (1.0, 1.0)$ m/s, the particle arrives at point B after going through 2 collisions, as shown in Figure 38A. The trajectory of centroid of particle resembles a single-period triangular wave. When $\mathbf{V}_0 = (1.0, 2.0)$ m/s, 4 collisions are needed to allow the particle to reach B, and the 2-period triangular wave is accurately predicted by PB-DDA, as shown in Figure 38B. If $\mathbf{V}_0 = (1.0, 3.0)$ m/s, the corresponding trajectory appears as the triangular wave with 3 periods, while the time of collisions is 6, as shown in Figure 38C. The example demonstrates that the principle of conservation of energy is strictly satisfied in the coupling of PB-DDA and FEM. This means that the node-based composition contact matrix is right and valid.

7.10 | Drop of a particle "chain"

Figure 39 further presents an example of particle "chain" to examine the validity of the particle/block-based composite contact matrix proposed by this study. A chain consisting of 2 star-shaped blocks and 9 smaller identical particles with a radius $r = 2.0$ m is considered, and springs are used to connect these particles/blocks. The particle "chain" is initially placed at a height of $H = 3.0$ m above a bigger static particle of radius $R = 8.0$ m. The gravity is then turned on for the "chain," leading its fall and impact on the bottom bigger particle. The acceleration of gravity $g = -10$ m/s^2, and the time step is set to be $\mathbf{\Delta} = 0.005$ second. All blocks and particles in the chain are assumed to be rigid bodies. The stiffness of

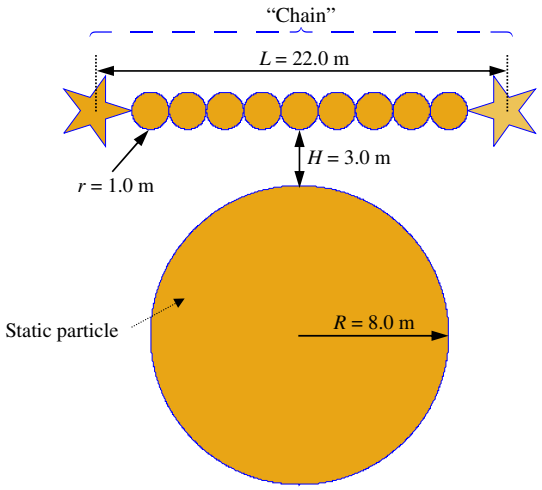

FIGURE 39 Configuration of a particle "chain" [Colour figure can be viewed at wileyonlinelibrary.com]

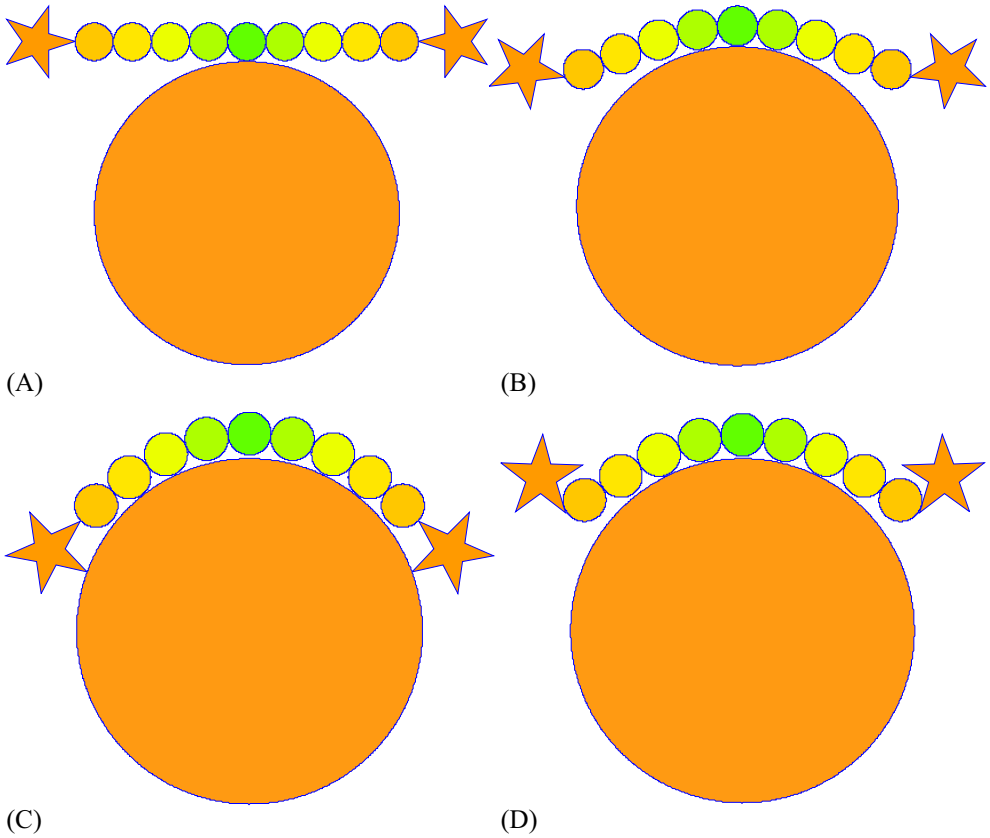

FIGURE 40 Movement of a "chain" obtained by particle-block discontinuous deformation analysis. A, CS = 155; B, CS = 200; C, CS = 263; D, CS = 540 [Colour figure can be viewed at wileyonlinelibrary.com]

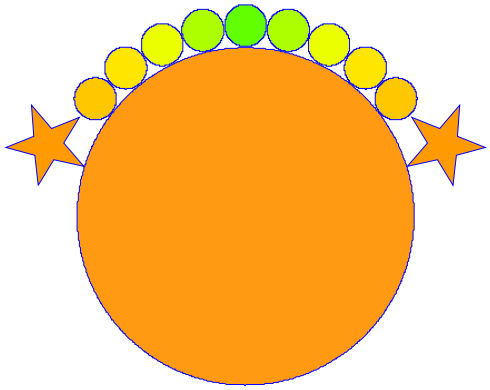

FIGURE 41 Final state of a "chain" obtained by particle-block discontinuous deformation analysis [Colour figure can be viewed at wileyonlinelibrary.com]

the 10 springs is equal to 0.5×10^{10} Pa. The 10 springs not only serve as the connectors but also play a role of energy absorbers. The dynamic behavior of the "chain" is examined. When CS = 155, the "chain" touches the bottom static particle, as shown in Figure 40A. While the middle part of the "chain" rebounds slightly, its 2 ends continue to move down accompanied by rotation, as shown in Figure 40B. At CS = 263, the 2 stars impact on the bigger particle, as shown in Figure 40C and then start to bounce back. Figure 40D shows the position of the "chain" at CS = 540. After a long time, due to the loss of kinetic energy, the "chain" settles down on the bigger particle, as shown in Figure 41.

From this example, we can safely conclude that the dynamic behavior of the "chain" can be captured by the governing equation with the particle/block-based composite contact matrix.

8 | CONCLUSIONS

A new comprehensive framework of DDA has been proposed to simulate discrete particle-block systems wherein rigid and nonrigid circle particles, ring-shaped particles, arbitrary-shaped block, and various complicated contact types among them have been rigorously integrated. The mechanics of rolling resistance and the tensile resistance at cemented interface have also been carefully considered, with their equivalent variational or quasivariational inequality formulations in conjunction with constraint conditions on the normal and shear contacts being incorporated into the framework. The following apparent benefits are gained through the new formulations of the DDA framework toward modeling a discrete particle-block system. (i) It helps get rid of the necessity of artificial springs in coping with potential interactions occurring between individual bodies, which, otherwise, are always needed in other DDA methods. (ii) The existing formulas governing the link, spring, and beam elements in FEM are exploited to establish the relevant controlling equations in PB-DDA using the simple transformation matrices, which help bypass complicated mathematical derivations. (iii) The node-based composite contact matrix derived for coupled modeling of PB-DDA and FEM may help enhance the accuracy of predicted stresses and strains. (iv) The particle/block-based composite contact matrix obtained in this study enables the proposed PB-DDA to retain all functions of the original DDA while broadening its application range. The accuracy and effectiveness of the proposed new DDA framework have been validated through a wide variety of demonstrated examples. Next, we will extend the proposed DDA framework to 3-dimensional cases and investigate the corresponding parallel algorithm.

ACKNOWLEDGEMENTS

This study was partially supported by the University Grants Council of Hong Kong through a Collaborative Research Fund (CRF) under project C6012-15G. This study was also supported by the 973 Program of the National Basic Research Program of China under grant 2014CB047100 and the National Natural Science Foundation of China under grants 11172313 and 51538001.

ORCID

Huo Fan http://orcid.org/0000-0001-5432-5642

REFERENCES

1. Fermi E, Pasta J, Ulam S. Studies of nonlinear problems. Los Alamos Report LA-1940. 1955; 978.
2. Alder BJ, Wainwright TE. Studies in molecular dynamics. I. General method. *J Chem Phys*. 1959;31(2):459-466.
3. Rahman A. Correlations in the motion of atoms in liquid argon. *Phys Rev*. 1964;136(2A):A405.
4. Rapaport DC, Blumberg RL, McKay SR, Christian W. The art of molecular dynamics simulation. *Comput Phys*. 1996;10(5):456-456.
5. Hamelberg D, Mongan J, McCammon JA. Accelerated molecular dynamics: a promising and efficient simulation method for biomolecules. *J Chem Phys*. 2004;120(24):11919-11929.
6. Hospital A, Goñi JR, Orozco M, Gelpi JL. Molecular dynamics simulations: advances and applications. *Adv Appl Bioinform Chem*. 2015;8:37-47.
7. Chen SY, Doolen GD. Lattice Boltzmann method for fluid flows. *Annu Rev Fluid Mech*. 1998;30(1):329-364.
8. Lallemand P, Luo LS. Theory of the lattice Boltzmann method: dispersion, dissipation, isotropy, Galilean invariance, and stability. *Phys Rev E*. 2000;61(6):6546.
9. Aidun CK, Clausen JR. Lattice-Boltzmann method for complex flows. *Annu Rev Fluid Mech*. 2010;42:439-472.
10. Fan H, Zheng H. MRT-LBM-based numerical simulation of seepage flow through fractal fracture networks. *Sci China Technol Sci*. 2013;56(12):3115-3122.
11. Krüger T, Kusumaatmaja H, Kuzmin A, Shardt O, Silva G, Viggen EM. *The Lattice Boltzmann Method: Principles and Practice*. Cham, Switzerland: Springer; 2016.
12. Cundall PA, Strack ODL. A discrete numerical model for granular assemblies. *Geotechnique*. 1979;29(1):47-65.
13. Cundall PA, Strack ODL. The development of constitutive laws for soil using the distinct element method. *Numer Methods Geomech*. 1979;1:289-317.
14. Cundall PA. Distinct element models of rock and soil structure. *Anal Comput Methods Eng Rock Mech*. 1987;129-163.
15. Cundall PA, Hart RD. Numerical modelling of discontinua. *Eng Comput*. 1992;9(2):101-113.
16. Williams JR, O'Connor R. Discrete element simulation and the contact problem. *Arch Comput Methods Eng*. 1999;6(4):279-304.
17. Coetzee CJ. Calibration of the discrete element method. *Powder Technol*. 2017;310:104-142
18. Munjiza A, Owen DRJ, Bicanic N. A combined finite-discrete element method in transient dynamics of fracturing solids. *Eng Comput*. 1995;12(2):145-174.
19. Munjiza A, Andrews KRF, White JK. Combined single and smeared crack model in combined finite-discrete element analysis. *Int J Numer Methods Eng*. 1999;44(1):41-57.
20. Munjiza AA. *The Combined Finite-Discrete Element Method*. Chichester, UK: John Wiley & Sons; 2004.
21. Rougier E, Munjiza A, John NWM. Numerical comparison of some explicit time integration schemes used in DEM, FEM/DEM and molecular dynamics. *Int J Numer Methods Eng*. 2004;61(6):856-879.
22. Zhu HP, Zhou ZY, Yang RY, Yu AB. Discrete particle simulation of particulate systems: theoretical developments. *Chem Eng Sci*. 2007;62(13):3378-3396.
23. Rougier E, Knight EE, Broome ST, Sussman AJ, Munjiza A. Validation of a three-dimensional finite-discrete element method using experimental results of the split Hopkinson pressure bar test. *Int J Rock Mech Min Sci*. 2014;70:101-108.
24. Lei Z, Rougier E, Knight EE, Munjiza A. A framework for grand scale parallelization of the combined finite discrete element method in 2D. *Comput Part Mech*. 2014;1(3):307-319.
25. Lei Z, Rougier E, Knight EE, Munjiza A, Viswanathan H. A generalized anisotropic deformation formulation for geomaterials. *Comput Part Mech*. 2016;3(2):215-228.
26. Perkins E, Williams JR. A fast contact detection algorithm insensitive to object sizes. *Eng Comput*. 2001;18(1/2):48-62.
27. Williams JR, Perkins E, Cook B. A contact algorithm for partitioning *N* arbitrary sized objects. *Eng Comput*. 2004;21(2/3/4):235-248.
28. Williams JR, Holmes D, Tilke P. Parallel computation particle methods for multi-phase fluid flow with application oil reservoir characterization. In: *Particle-Based Methods*. Dordrecht, The Netherlands: Springer; 2011:113-134.
29. Munjiza A, Knight EE, Rougier E. *Computational mechanics of discontinua*. Chichester, UK: John Wiley & Sons; 2011.
30. Munjiza A, Knight EE, Rougier E. *Large Strain Finite Element Method: A Practical Course*. Chichester, UK: John Wiley & Sons; 2015.
31. Shi GH. Discontinuous Deformation Analysis: A New Numerical Model for the Statics and Dynamics of Block System [PhD thesis]. Berkeley, California: University of California Berkeley; 1988.
32. Shyu K. Nodal-Based Discontinuous Deformation Analysis [PhD thesis]. Berkeley, California: University of California Berkeley; 1993.
33. Cheng YM, Zhang YH. Coupling of FEM and DDA methods. *Int J Geomech*. 2002;2(4):503-517.
34. Ke TC. The issue of rigid body rotation in DDA. Paper presented at: Proceedings of the First International Forum on Discontinuous Deformation Analysis (DDA) and Simulation of Discontinuous Media; 1996; Berkeley, CA.
35. MacLaughlin MM, Sitar N. Rigid body rotation in DDA. Paper presented at: Proceedings of the First International Forum on Discontinuous Deformation Analysis (DDA) and Simulation of Discontinuous Media; 1996; Berkeley, CA.

36. Cheng YM, Zhang YH. Rigid body rotation and block internal discretization in DDA analysis. *Int J Numer Anal Methods Geomech*. 2000;24(6):567-578.
37. Jiang W, Zheng H. An efficient remedy for the false volume expansion of DDA when simulating large rotation. *Comput Geotech*. 2015;70:18-23.
38. Fan H, Zheng H, Zhao JD. Discontinuous deformation analysis based on strain-rotation decomposition. *Int J Rock Mech Min Sci*. 2017;92:19-29.
39. Fan H, Zheng H, Zhao JD. Three-dimensional discontinuous deformation analysis based on strain-rotation decomposition. *Comput Geotech*. 2018;95:191-210.
40. Zhi-Da C. On the representation of finite rotation in nonlinear field theory of continuum mechanics. *Appl Math Mech*. 1986;7(11):1017-1026.
41. Zhong Q, Zhi-Da C. Large deformation analysis of shells with finite element method based on the S-R decomposition theorem. *Comput Struct*. 1988;30(4):957-961.
42. Li P, Zhi-Da C. The updated co-moving coordinate formulation of continuum mechanics based on the S-R decomposition theorem. *Comput Methods Appl Mech Eng*. 1994;114(1-2):21-34.
43. Lin CT, Amadei B, Jung J, Dwyer J. Extensions of discontinuous deformation analysis for jointed rock masses. *Int J Rock Mech Min Sci*. 1996;33(7):671-694.
44. Cai YE, Liang GP, Shi GH, Cook NGW. Studying an impact problem by using LDDA method. Paper presented at: Proceedings of the First International Forum on Discontinuous Deformation Analysis (DDA) and Simulations of Discontinuous Media; 1996; Berkeley, CA.
45. Zheng H, Jiang W. Discontinuous deformation analysis based on complementary theory. *Sci China Technol Sci*. 2009;52(9):2547-2554.
46. Zheng H, Li XK. Mixed linear complementarity formulation of discontinuous deformation analysis. *Int J Rock Mech Min Sci*. 2015;75:23-32.
47. Li XK, Zheng H. Condensed form of complementarity formulation for discontinuous deformation analysis. *Sci China Technol Sci*. 2015;58(9):1509-1519.
48. Jiang W, Zheng H. Discontinuous deformation analysis based on variational inequality theory. *Int J Comput Methods*. 2011;8(02):193-208.
49. Fan H, He SM. An angle-based method dealing with vertex-vertex contact in the two-dimensional discontinuous deformation analysis (DDA). *Rock Mech Rock Eng*. 2015;48(5):2031-2043.
50. Shi GH. Contact theory. *Sci China Technol Sci*. 2015;58(9):1450-1496.
51. Fan H, Zheng H, Wang JF. A generalized contact potential and its application in discontinuous deformation analysis. *Comput Geotech*. 2018;99:104-114.
52. Shi GH. Simplex integration for manifold method, FEM, DDA and analytical analysis. Paper presented at: Proceedings of the First International Forum on Discontinuous Deformation Analysis, DDA and Simulations of Discontinuous Media; 1996; Berkeley, CA.
53. Ke TC, Bray J. Modeling of particulate media using discontinuous deformation analysis. *J Eng Mech*. 1995;121(11):1234-1243.
54. Beyabanaki SAR, Bagtzoglou AC. Non-rigid disk-based DDA with a new contact model. *Comput Geotech*. 2013;49:25-35.
55. Koo CY, Chern JC. Modification of the DDA method for rigid block problems. *Int J Rock Mech Min Sci*. 1998;35(6):683-693.
56. Zheng H, Zhang P, Du XL. Dual form of discontinuous deformation analysis. *Comput Methods Appl Mech Eng*. 2016;305:196-216.
57. Potyondy DO, Cundall PA. A bonded-particle model for rock. *Int J Rock Mech Min Sci*. 2004;41(8):1329-1364.
58. Obermayr M, Dressler K, Vrettos C, Eberhard P. A bonded-particle model for cemented sand. *Comput Geotech*. 2013;49:299-313.
59. Cho N, Martin CD, Sego DC. A clumped particle model for rock. *Int J Rock Mech Min Sci*. 2007;44(7):997-1010.
60. Turichshev A, Hadjigeorgiou J. Development of synthetic rock mass bonded block models to simulate the behaviour of intact veined rock. *Geotech Geol Eng*. 2017;35(1):313-335.
61. Antman SS. The influence of elasticity on analysis: modern developments. *Bull Am Math Soc*. 1983;9(3):267-291.
62. Facchinei F, Pang JS. *Finite-Dimensional Variational Inequalities and Complementary Problems*. New York, NY: Springer; 2003.
63. Newmark NM. A method of computation for structural dynamics. *J Eng Mech Div*. 1959;85(3):67-94.
64. He BS, Liao LZ. Improvements of some projection methods for monotone nonlinear variational inequalities. *J Optim Theory Appl*. 2002;112(1):111-128.
65. Zhang YB, Xu Q, Chen GQ, Zhao XJ, Zheng L. Extension of discontinuous deformation analysis and application in cohesive-frictional slope analysis. *Int J Rock Mech Min Sci*. 2014;70:533-545.
66. Zienkiewicz OC, Taylor RL, Zhu JZ. *The Finite Element Method: Its Basis and Fundamentals*. 7th ed. Oxford, UK: Elsevier: Butterworth-Heinemann; 2013.
67. Zhu BF. *The Principle and Application of Finite Element Method*. 3rd ed. Beijing, China: China Water Power Press; 2009. [in Chinese].
68. Fan H, Zheng H, He SM, Jiang Z. A novel numerical manifold method with derivative degrees of freedom and without linear dependence. *Eng Anal Bound Elem*. 2016;64:19-37.
69. Fan H, Zheng H, He SM. S-R decomposition based numerical manifold method. *Comput Methods Appl Mech Eng*. 2016;304:452-478.

How to cite this article: Fan H, Zhao J, Zheng H. Variational inequality-based framework of discontinuous deformation analysis. *Int J Numer Methods Eng*. 2018;115:358–394. https://doi.org/10.1002/nme.5807

APPENDIX

DERIVATION OF MATRICES GOVERNING RIGID OR DEFORMABLE CIRCLE OR RING PARTICLES

Take a deformable ring, as shown in Figure A1, as an example, where R_E and R_I are the external and inner diameters of the ring, respectively. The rectangular coordinate system X-Y is global, while the coordinate system x-y is the local coordinate system with taking the centroid C(X_c, Y_c) of the ring as the origin of coordinates. Note that *x-axis* is meanwhile the polar axis of local polar coordinates.

A.1 | Submatrix of stiffness

The stiffness submatrix can be expressed in the following general form:

$$\mathbf{K}_P = \iint \mathbf{B}^T\mathbf{D}\mathbf{B}\mathrm{d}X\mathrm{d}Y, \tag{A.1}$$

where

$$\mathbf{D} = \begin{bmatrix} 0 & 0 & 0 & 1 \\ 0 & 0 & 0 & 1 \end{bmatrix}, \tag{A.2}$$

and

$$\mathbf{E} = \frac{E}{1-\upsilon^2}\begin{bmatrix} 1 & \upsilon \\ \upsilon & 1 \end{bmatrix}, \tag{A.3}$$

where E and υ are the Young's modulus and Poisson's ratio, respectively. In consideration of Equations (A.2) and (A.3), Equation (A.1) can be recast into

$$\mathbf{K}_P = \frac{\pi E\left(R_E^2 - R_I^2\right)}{1-\upsilon}\begin{bmatrix} 0 & 0 & 0 & 0 \\ 0 & 0 & 0 & 0 \\ 0 & 0 & 0 & 0 \\ 0 & 0 & 0 & 1 \end{bmatrix}. \tag{A.4}$$

A.2 | Submatrix of mass

The mass submatrix can be generally written as

$$\mathbf{M}_P = \iint \mathbf{T}^T\mathbf{T}\mathrm{d}X\mathrm{d}Y, \tag{A.5}$$

where $\mathbf{T}$ is the interpolation shape function. The relationship between the global coordinate system X-Y and the local coordinate system x-y reads

$$\begin{aligned} X &= x + X_c \\ Y &= y + Y_c \end{aligned}. \tag{A.6}$$

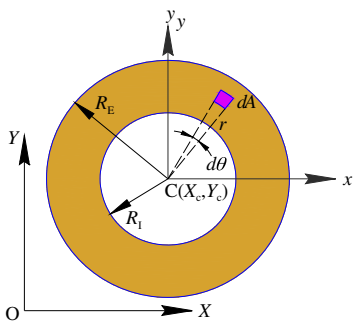

FIGURE A1 A deformable ring [Colour figure can be viewed at wileyonlinelibrary.com]

The relationship between the polar coordinates and the local rectangular coordinates is given by

$$\begin{aligned} x &= r\cos\theta \\ y &= r\sin\theta, \end{aligned} \tag{A.7}$$

where (r, θ) is the polar coordinate of any point in ring. For an infinitesimal area dA, we have

$$dA = \mathrm{d}X\mathrm{d}Y = \mathrm{d}x\mathrm{d}y = r\mathrm{d}r\mathrm{d}\theta. \tag{A.8}$$

Using Equations (A.6) to (A.8) yields

$$\mathbf{M}_{\mathrm{P}} = \begin{bmatrix} g_1 & 0 & 0 & 0 \\ 0 & g_1 & 0 & 0 \\ 0 & 0 & g_2 & 0 \\ 0 & 0 & 0 & g_2 \end{bmatrix}, \tag{A.9}$$

where

$$g_1 = \pi\left(R_{\mathrm{E}}^2 - R_{\mathrm{I}}^2\right), \quad g_2 = \pi\left(R_{\mathrm{E}}^4 - R_{\mathrm{I}}^4\right)/2. \tag{A.10}$$

A.3 | Submatrix of initial stress

The initial stress submatrix generally presents the following form:

$$\mathbf{f}_{\sigma_0} = \iint \mathbf{B}^{\mathrm{T}} \begin{bmatrix} \sigma_0 \\ \sigma_0 \end{bmatrix} \mathrm{d}X\mathrm{d}Y, \tag{A.11}$$

where σ_0 is the initial stress. Substituting Equation (A.2) into Equation (A.11) leads to

$$\mathbf{f}_{\sigma_0} = 2\pi\left(R_{\mathrm{E}}^2 - R_{\mathrm{I}}^2\right) \begin{bmatrix} 0 \\ 0 \\ 0 \\ \sigma_0 \end{bmatrix}. \tag{A.12}$$

A.4 | Submatrix of body force

The body force submatrix is written as

$$\mathbf{f}_{\mathrm{body}} = \iint \mathbf{T}^{\mathrm{T}} \begin{bmatrix} f_X \\ f_Y \end{bmatrix} \mathrm{d}X\mathrm{d}Y, \tag{A.13}$$

where f_X and f_Y are 2 components of body force. Substituting Equation (A.2) into Equation (A.11) and considering Equations (A.7) and (A.8) yields

$$\mathbf{f}_{\mathrm{body}} = \pi\left(R_{\mathrm{E}}^2 - R_{\mathrm{I}}^2\right) \begin{bmatrix} f_X \\ f_Y \\ 0 \\ 0 \end{bmatrix}. \tag{A.14}$$